nature communications

Article

https://doi.org/10.1038/s41467-025-67086-9

A protein complex in the extreme distal tip of vertebrate motile cilia controls their organization, length, and function

Received: 16 June 2025

Accepted: 20 November 2025

Juyeon Hong[1,2,10], **Chanjae Lee**[1,10], **Gopika Madhu**[3,10], **Ophelia Papoulas**[1,10], **Ece Atayeter**[1,10], **Gabriel Hoogerbrugge**[1,10], **Jiehong Pan**[4,10], **Maki Takagishi**[5,10], **Nadia I. Manzi**[1,10], **Daniel J. Dickinson**[1,10], **Amjad Horani**[6,10], **Steven L. Brody**[4,10], **Edward M. Marcotte**[1,10], **Vivek N. Prakash**[3,7,8,10], **Tae Joo Park**[2,9,10] ✉ & **John B. Wallingford**[1,10] ✉

The beating of cilia on multi-ciliated cells (MCCs) is essential for normal development and homeostasis in animals. But while the structure and function of basal bodies and axonemes have received significant attention recently, the distal tips of MCC cilia remain relatively poorly defined. Here, we characterize the molecular organization of the distal tip of vertebrate MCC cilia, characterizing two distinct domains occupied by distinct protein constituents. Using frog, mouse, and human MCCs, we find that two largely uncharacterized proteins, Ccdc78 and Ccdc33, occupy a previously undefined region at the extreme distal tip, and these are required for the normal organization of all other known tip proteins. Ccdc78 and Ccdc33 each display robust microtubule-bundling activity both in vivo and in vitro, yet each is independently required for normal length regulation of MCC cilia. Moreover, loss of each protein elicits a distinct pattern of defective cilia beating and resultant fluid flow. Thus, two previously undefined proteins form a key module essential for organizing and stabilizing the distal tip of motile cilia in vertebrate MCCs. We propose that these ill-defined proteins represent potential disease loci for motile ciliopathies.

Motile cilia are microtubule-based organelles conserved across the eukaryotes and play important roles in development and homeostasis. Motile cilia on multi-ciliated cells (MCCs) generate fluid flow to clear mucus in the airways, to transport gametes in the reproductive tracts, and to move cerebrospinal fluid in the central nervous system (Fig. 1A)[1,2]. Dysfunction of ciliary motility in MCCs causes primary ciliary dyskinesia (PCD), an incurable genetic disease characterized by chronic respiratory

---

[1]Department of Molecular Biosciences, University of Texas at Austin, Austin, Texas, USA. [2]Department of Biological Sciences, Ulsan National Institute of Science and Technology, Ulsan, South Korea. [3]Department of Physics, College of Arts and Sciences, University of Miami, Coral Gables, FL, USA. [4]Division of Pulmonary and Critical Care Medicine, Department of Medicine, Washington University School of Medicine in St. Louis, Saint Louis, MO, USA. [5]Dept. of Medicinal and Life Sciences, Nagoya City University, Nagoya, Japan. [6]Department of Pediatrics, Washington University School of Medicine in St. Louis, Saint Louis, MO, USA. [7]Dept. of Biology, College of Arts and Sciences, University of Miami, Coral Gables, FL, USA. [8]Department of Marine Biology and Ecology, Rosenstiel School of Marine, Atmospheric and Earth Science, University of Miami, Coral Gables, FL, USA. [9]Center for Genomic Integrity, Institute for Basic Science, Ulsan, Republic of Korea. [10]These authors contributed equally: Juyeon Hong, Chanjae Lee, Gopika Madhu, Ophelia Papoulas, Ece Atayeter, Gabriel Hoogerbrugge, Jiehong Pan, Maki Takagishi, Nadia I. Manzi, Daniel J. Dickinson, Amjad Horani, Steven L. Brody, Edward M. Marcotte, Vivek N. Prakash, Tae Joo Park, John B. Wallingford. ✉e-mail: parktj@unist.ac.kr; Wallingford@austin.utexas.edu

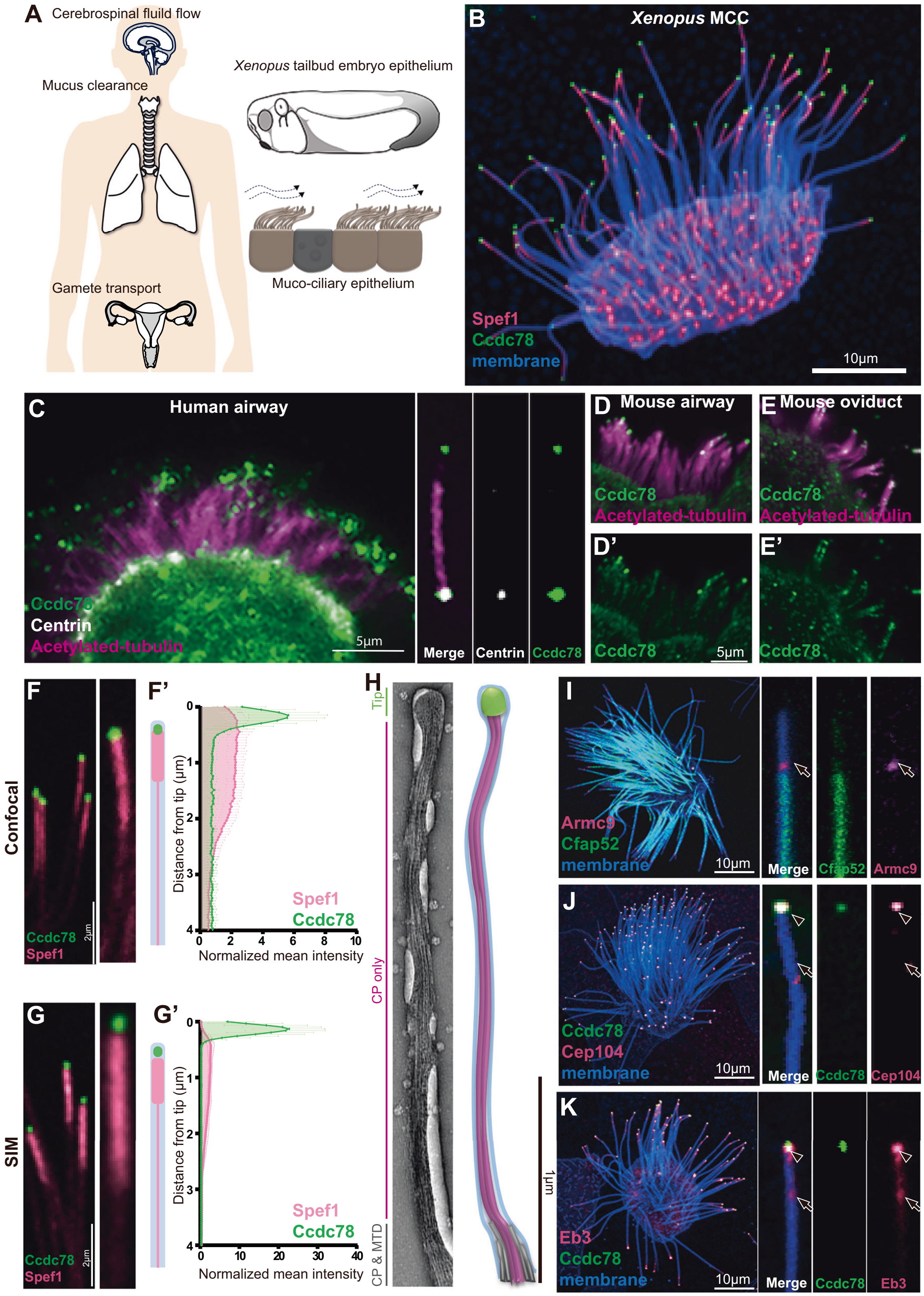

tract infection leading to bronchiectasis, as well as infertility and hydrocephalus[3–5].

Motile cilia in MCCs are unique for their myriad well-described specializations, from the rootlets and basal feet anchoring basal bodies to the carefully patterned positions of dynein motors along the axoneme[2]. Far less is known, however, about the specializations at the distal tips of MCC cilia[6]. This dearth of knowledge stems in part from the fact that these structures are far more variable than other elements of motile cilia. Indeed, tip structures vary between species, between different tissues, and even between developmental stages of an organism[6]. In MCCs, the ends of all microtubules (doublets, singlets, and central pair) are each "capped" by ill-defined structures variously called caps or plugs[6–8]. The molecular nature of such structures in vertebrate MCCs is not known.

Fig. 1 | Establishing distal ciliary domain in vertebrate MCC. A Schematic representations of the role of MCCs in the human brain, respiratory tract and reproductive system. The tailbud stage of *Xenopus* embryo is covered by mucociliary epithelium, which resembles mammalian MCCs. **B** Image of *Xenopus* MCC labeled with Spef1-RFP (magenta), GFP-Ccdc78 (green) and membrane-BFP (blue). Scale bar represents 10 µm. **C** Immunofluorescence image of human trachea epithelial cell (HTEC) stained with anti-acetylated tubulin (magenta), anti-CCDC78 (green) and anti-CENTRIN (gray). The image of single cilium scraped from HTEC is shown on the right. Scale bar represents 5 µm. **D**, **E** Imaging of mouse airway MCCs (D, D′) and oviduct MCCs (E, E′) stained with anti-acetylated tubulin (magenta) and anti-CCDC78 (green). Scale bars represent 5 µm. **F** Confocal image of cilia labeled with GFP-Ccdc78 (green) and Spef1-RFP (magenta), magnified view of the cilium on the right with cartoon. (F′) Quantification of fluorescent intensity along the axoneme shown in right, the mean intensity was normalized by average intensity ($n = 40$ cilia, 10 cells, 4 embryos, 2 experiments). Data are presented as mean values +/- SD. We quantified its localization in *Xenopus* by measuring signal intensity in the distal-most four microns of individual cilia, which allowed us to ignore confounding signals as crowded cilia lay cross one another more proximally on MCCs. **G** Structural illumination microscopy (SIM) image of cilia labeled with GFP-Ccdc78 (green) and Spef1-RFP (magenta), magnified view of the cilium on the right with cartoon. (G′) Quantification of fluorescent intensity along the axoneme shown in right (see Methods)($n = 50$ cilia, 10cells, 3 embryos, 2 experiments). Data are presented as mean values +/- SD. **H** TEM image of negatively stained *Xenopus* embryo MCC cilia with schematic model of same cilium. The tip is in green, central pair (CP) in pink and microtubule doublet (MTD) in gray. **I** Localization of mScarlet3-Armc9 (magenta, arrow) with GFP-Cfap52 (green) in a single MCC with a magnified single cilium from same cell shown at right. **J** Localization of mScarlet3-Ccdc78 (green) with GFP-Cep104 (magenta, arrowhead and arrow) in a single MCC with a magnified single cilium from same cell shown on right. **K** Localization of mScarlet3-Ccdc78 (green) with GFP-Eb3 (magenta, arrowhead and arrow) in a single MCC with a magnified single cilium from same cell shown at right.

Unlike vertebrate MCC cilia, the distal tips of motile cilia in unicellular organisms have recently been resolved by cryo-EM (cryo-electron microscopy). In *Tetrahymena*, for example, the distal-most region of the axoneme is occupied only by the central pair, preceded by a region that also contains A-tubule singlets, with the normal 9 + 2 architecture finally arising about a micron proximal to the tip[9–11]. Electron microscopy studies reveal a similar configuration in *Chlamydomonas*[12–17]. The fine structure of the tips of motile cilia in vertebrate MCCs is less defined[7,18–20], but studies of protein localization provide entry points for understanding.

For example, end-binding proteins that localize to MT plus ends, such as Eb1 and Eb3, label the tips of both primary and motile cilia in vertebrates[21–24]. Other proteins label specifically the tips of motile cilia, for example, the MT-bundling protein Spef1 localizes to the central pair apparatus along the length of the axoneme[9,25] but is dramatically enriched in the tips of *Xenopus*, mouse and human MCC cilia[24,26,27]. That said, other tip proteins described in unicellular organisms, such as Armc9 and Cep104[9–11] have yet to be resolved clearly in vertebrate MCCs. How these proteins are recruited and arranged in distal cilia remains poorly defined.

Here, we combine confocal, structured illumination, and electron microscopy to provide a quantitative description of the molecular organization of the distal tips of vertebrate MCC cilia. We find that the poorly defined proteins Ccdc78 and Ccdc33 occupy a conserved, specialized domain in the extreme distal tip of MCC cilia in *Xenopus*, mouse, and human. This region is distal to and distinct from that previously associated with other ciliary tip proteins such as Spef1. In vivo and in vitro assays reveal that Ccdc78 and Ccdc33 act in concert to bundle microtubules, suggesting they stabilize the cilia tip. Despite this shared activity, these proteins nonetheless play non-redundant roles in maintaining the normal localization of all other tip proteins, and loss of Ccdc78 or Ccdc33 elicits distinct defects in overall cilia length control. These, in turn, elicit distinct effects on cilia beating and resultant fluid flow. We conclude that Ccdc78 and Ccdc33 represent a module that organizes and stabilizes the architecture of the distal tip of motile cilia in vertebrate MCCs, thereby ensuring robust and effective cilia-mediated fluid flow.

Results

Ccdc78 defines a distinct domain at the extreme distal tip of MCC motile cilia

The MCCs of the *Xenopus* embryo epidermis accurately reflect the biology of mammalian MCCs[28] (Fig. 1A), and we have exploited these very large cilia as a platform for screening the localization of poorly understood proteins[27,29]. Recently, we observed that Ccdc78 specifically marked the tips of motile cilia (Fig. 1B). This pattern of localization was observed with both N- and C-terminal GFP fusions both during ciliogenesis and in mature cilia (Supplementary Fig. 1A). Ccdc78 was previously implicated in the biogenesis of basal bodies in MCCs[30,31], and as expected, our GFP fusion also marked deuterosomes in the MCC cytoplasm as well as foci on the apical surface (Supplementary Fig. 1A, B).

Ccdc78 is composed entirely of coiled-coil domains and is highly conserved among vertebrates. A distantly related Ccdc78 orthologue has been observed in the distal tips of motile cilia in *Tetrahymena*, but that protein contains not only coiled coils but also a kinesin domain[10]. We therefore asked if distal tip localization is a conserved feature of vertebrate Ccdc78 using immunostaining for the endogenous protein. In primary human tracheal MCCs, CCDC78 was present at cilia tips and in the apical cytoplasm (Fig. 1C, Supplementary Fig. 2A). In single cilia scraped from human MCCs, CCDC78 was enriched at both ends and was co-localized with centrin proximally (Fig. 1C). Imaging of MCCs in the mouse airway and oviduct suggests a similar tip localization (Fig. 1D, E; Supplementary Fig. 2B).

The domain in cilia tips marked by Ccdc78 localization was clearly distinct from that of previously described proteins such as Spef1, which is also enriched distally in MCC cilia in humans, mice, and *Xenopus*[24,26,27]. Spef1 marks an elongate domain, while Ccdc78 was far more restricted, marking a roughly circular domain in the extreme distal tip (Fig. 1B, F). Structured illumination super-resolution microscopy indicated that the regions marked by Spef1 and Ccdc78 enrichment were largely non-overlapping (Fig. 1G). To quantify these regions, we measured pixel intensity for each marker along the distal four microns of cilia, since frequent overlap of the densely packed axonemes on MCCs made intensity measurements of more proximal regions impossible. Quantification in both confocal and structured illumination microscopy indicated that while Spef1 is enriched in the distal 2.25 microns, Ccdc78 was restricted to the most distal <0.2 microns (Fig. 1F′, G′).

In vertebrate MCCs, motile cilia are characterized by a conserved structure of nine outer doublets and two microtubules forming a central pair (9 + 2) that runs along the axoneme length. However, the structure of the distal tips of motile cilia varies widely between species and even cell types[6] and the ultrastructure of the tips of *Xenopus* epidermal MCCs is unknown. Using negative stain electron microscopy (EM), we consistently observed that the extreme distal tip was characterized by a bulb-like structure occupying roughly the final 0.15 (+ /− 0.02) microns of each cilium (Fig. 1H, green; Supplementary Fig. 3A). This bulb was followed proximally by a narrow "neck" region roughly 2.2 microns in length (Fig. 1H, pink; Supplementary Fig. 3B), after which point the axoneme quickly widens (Fig. 1H, gray).

The size and position of the distal bulb observed in EM precisely match that of the region marked by Ccdc78, while the neck region precisely matches that of Spef1 (Fig. 1F–H). Given that Spef1 interacts specifically with central pair microtubules[9,25], we interpret the two-micron-long neck region in our EM as a central pair extension similar to that described at the distal ends of 9 + 2 cilia of *Tetrahymena*[9–11]. Our data thus suggest that the outer doublets of *Xenopus* MCC cilia terminate roughly 2.25 microns from the cilia tip (Fig. 1H, bottom of panel, gray).

To confirm this interpretation, we labeled *Xenopus* MCCs with Armc9, which localizes to the distal ends of the outer doublet B-tubules in *Tetrahymena*[10,11] and Cfap52, a microtubule inner protein localized along the length of B-tubules in bovine tracheal MCCs[32]. In *Xenopus*, Armc9 labeled a small region precisely corresponding with the distal end of the Cfap52 domain, and this region fell precisely 2.2 microns from the tip (Fig.1I, arrow; quantified in Supplementary Fig. 3C).

As a final test, we examined the localization of Cep104 and Eb3, each of which marks the distal ends of both central pair and doublet microtubules[22,23,33,34]. Each protein marked two regions in *Xenopus* MCCs, the extreme distal tip marked by Ccdc78 and the region 2.2 microns from the tip that is marked by Armc9 (Fig. 1J-K, arrow, arrowhead; quantified in Supplementary Fig. 3D-E). From these data, we propose that the Ccdc78-positive bulb at the extreme tips of MCC cilia represents a distinct domain, which we propose to call the extreme distal tip (EDT). The EDT is bordered proximally in *Xenopus* by a central pair extension marked by Spef1, followed by the outer doublets roughly 2.2 microns from the tip.

Ccdc78 is required for localization of distal tip proteins in MCCs

To explore the function of Ccdc78, we performed knockdown (KD) using anti-sense morpholino oligonucleotides that efficiently disrupted the splicing of Ccdc78 (Supplementary Fig. 4A). Consistent with its known role in deuterosome function[30,31], Ccdc78 KD significantly reduced the number of basal bodies in MCCs (Supplementary Fig. 4B, C and E). This phenotype was rescued by re-expression of Ccdc78 (Supplementary Fig. 4D, E), confirming that the KD was specific.

Importantly, Ccdc78 KD also elicited loss of Spef1 enrichment from the distal axoneme (Fig. 2A, B, D), and this phenotype was also rescued by re-expression of Ccdc78 (Fig. 2C, D). To better understand this phenotype, we examined Cep104 and Eb3 localization, finding that the normal two peaks collapsed to a single peak for each marker after Ccdc78 KD, and this peak was positioned at the very distal end of cilia (Fig. 2E–H; Supplementary Fig. 3F–I). Moreover, the B-tubule-end protein Armc9, normally present in a single domain 2.2 microns proximal to the tip, was radically re-positioned, marking the very distal ends of cilia after Ccdc78 KD (Fig. 2I–L). These changes in the localization of Cep104 and Armc9 were rescued by re-expression of Ccdc78 (Supplementary Fig. 5A–C, F–H).

Together, these data suggest that Ccdc78 KD elicits loss of the entire distal domain that is normally marked by Spef1 and normally extends 2.2 microns beyond the Armc9 domain. We interpret these data to mean that after Ccdc78 KD, the central pair extension is eliminated and that outer doublet and central pair microtubules terminate together at the very end of these defective cilia.

Ccdc78 interacts physically and functionally with Ccdc33 in the MCC cilia tip

To gain insights into Ccdc78 function, we searched for interacting proteins using in vivo affinity purification from *Xenopus* MCCs and mass spectrometry (APMS). We used an MCC-specific α-tubulin promoter[35] to express either GFP or GFP-Ccdc78 specifically in MCCs; we then isolated presumptive mucociliary epithelium, cultured it until MCCs were fully developed[36,37], and performed APMS with anti-GFP beads (Fig. 3A). Compared to GFP alone, the most strongly enriched protein in the GFP-Ccdc78-expressing cells was the bait itself, demonstrating the efficacy of the method (Fig. 3B; Supplementary Data 1).

Consistent with Ccdc78's known role in the cytoplasm[30,31], Ccdc78 APMS enriched for several proteins acting at the base of cilia, including Nup205[38] and Tsga10[39,40] (Fig. 3B, green; Supplementary Data 1). Other interactors were consistent with the axonemal localization of Ccdc78, such as the IFT kinesin subunit Kifap3 (Fig. 3B, green; Supplementary Data 1). Our APMS did not, however, identify known vertebrate cilia tip proteins such as Spef1 or Eb3 (Supplementary Data 1).

Rather, the most highly enriched prey protein was the largely uncharacterized Ccdc33 (Fig. 3B, pink). We previously identified *ccdc33* as a direct target of the ciliary transcription factor Rfx2 and found it localized to axonemes[29,41], but another group has suggested the protein localizes to peroxisomes[42], and nothing is known of Ccdc33 function. We therefore confirmed the interaction using reciprocal APMS with Ccdc33 as bait and found that Ccdc78 was the most strongly co-enriched prey protein (Fig. 3C, pink). Cytoplasmic Ccdc78-interactors such as Nup205 and Tsga10 were not enriched in Ccdc33 APMS (Fig. 3C, green; Supplementary Data 2), consistent with Ccdc33 and Ccdc78 interacting specifically in the axoneme.

Consistent with this idea, GFP-Ccdc33 localized specifically to the EDT of cilia at all stages of ciliogenesis in *Xenopus* MCCs (Fig. 4A) and was not present in the MCC cytoplasm (Supplementary Fig. 6A, B). A similar result was observed for endogenous CCDC33 in human tracheal epithelial cells differentiated in culture (Fig. 4B; Supplementary Figs. 2C and 6C). Z-projection of co-stained human MCCs confirmed that endogenous CCDC33 and CCDC78 co-localized at cilia tips, while Ccdc78 alone was also enriched in the apical cytoplasm (Supplementary Fig. 6D).

The co-localization of Ccdc33 and Ccdc78 at the EDT prompted us to test for functional interactions. We found that Ccdc78 KD eliminated the localization of GFP-Ccdc33 from the EDT (Fig. 4C–F). This KD did not reduce total protein levels of GFP-Ccdc33 in western blots, suggesting a specific effect on localization (Supplementary Fig. 7A). Reciprocally, we developed KD reagents that disrupted splicing of Ccdc33 (Supplementary Fig. 7B), and these severely disrupted but did not eliminate the EDT localization of Ccdc78 (Fig. 4G–J, Supplementary Fig. 7C).

Moreover, Ccdc33 KD reduced but did not eliminate the Spef1-enriched distal domain (Fig. 5A, B and D). Other effects of Ccdc33 KD also paralleled those of Ccdc78 KD, with loss of the distal peaks of Cep104 and Eb3, and Armc9 now abutting the cilia tip (Fig. 5E–L; Supplementary Fig. 7D–G). These effects were rescued by the re-expression of Ccdc33 mRNA (Fig. 5C, D; Supplementary Fig. 5D, E, I, J), demonstrating the specificity of the KD. Unlike Ccdc78, however, Ccdc33 KD had no effect on basal body numbers (Supplementary Fig. 7H–J), again consistent with our proteomic and localization data suggesting Ccdc33 functions only at the cilia tip. Thus, Ccdc78 and Ccdc33 act in concert and non-redundantly to control the molecular architecture of the distal regions of vertebrate MCC cilia.

Ccdc78 and Ccdc33 display microtubule bundling activity in vivo and in vitro

As we considered the possible molecular functions of Ccdc78 and Ccdc33, we noted that Spef1 is known to bundle microtubules[25,43], which in turn is thought to protect cilia tips from the high levels of mechanical strain experienced during beating[44,45]. We therefore assessed microtubule bundling by Ccdc78 or Ccdc33.

To this end, we uniformly labeled cells in the *Xenopus* epidermis with membrane-BFP and the well-defined microtubule reporter GFP-EMTB[46,47]. We then mosaically overexpressed Ccdc78 in clones of cells marked by co-expressed membrane-RFP (Fig. 6A)[48]. We observed that membrane-RFP-positive clones displayed robust bundling of cytoplasmic microtubules that was not observed in cells outside the clone (Fig. 6B; Supplementary Fig. 8A and C–E). Mosaic expression of Ccdc33 elicited the same effect (Fig. 6C; Supplementary Figs. 8B and C–E).

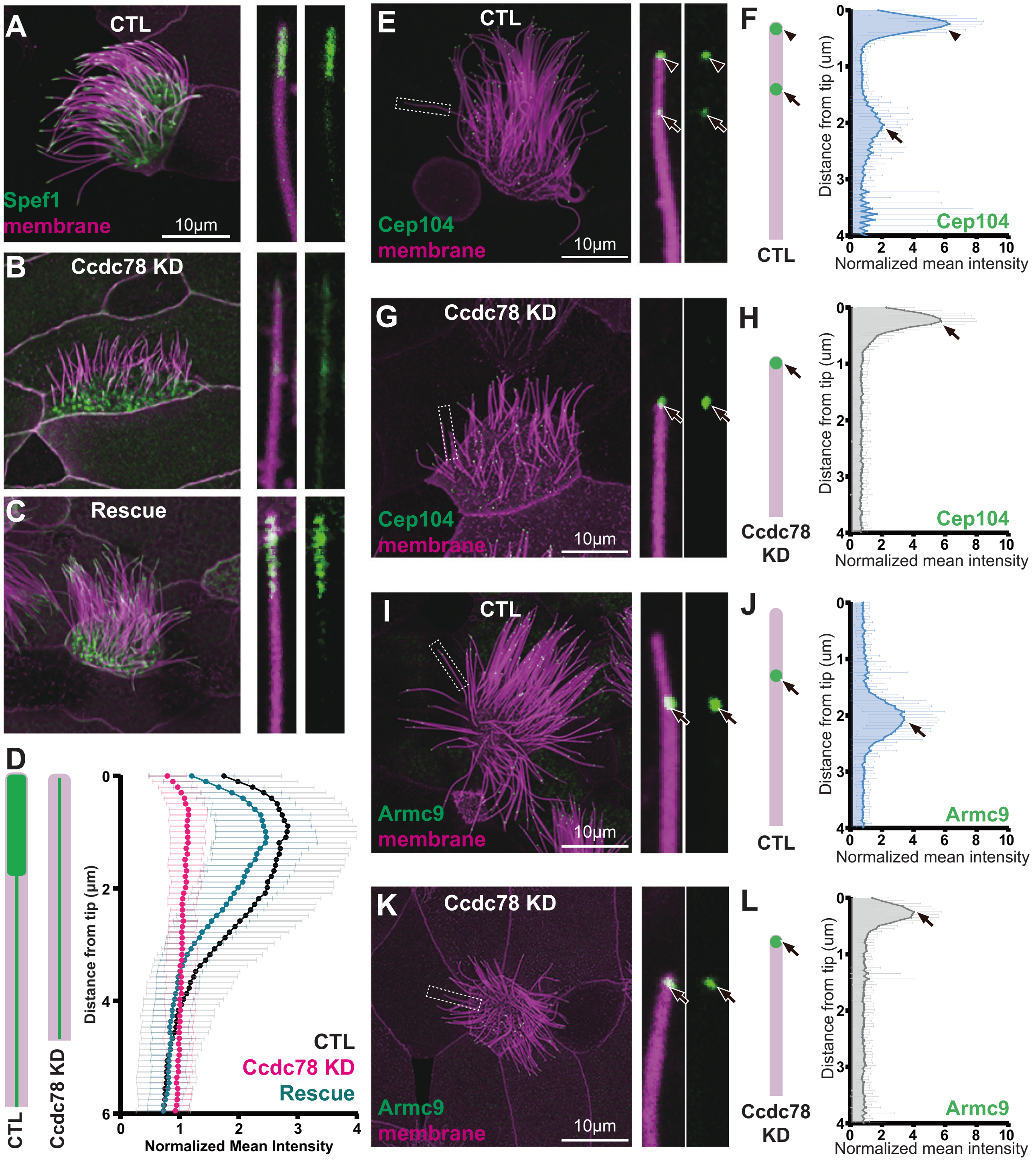

Fig. 2 | Ccdc78 is required for localization of distal tip proteins in MCCs. **A–C** Image of GFP-Spef1 (green) and membrane-RFP (magenta) in *Xenopus* MCCs in control **A**, Ccdc78 MO-injected **B** or rescued embryos **C** with magnified view of cilium on the right. Scale bars represent 10 µm. **D** Schematic cartoon of Spef1 distribution in control and Ccdc78 MO-injected cilium. Quantification of fluorescent intensity of GFP-Spef1 along the axoneme was normalized by average intensity in control, Ccdc78 MO injected and rescued embryos. (*n* = 154 cilia, 45 cells, 9 embryos, 3 experiments) Data are presented as mean values +/- SD.**E**–H Localization of distal proteins in control (**E**, **F**) and Ccdc78 MO injected (**G**, **H**) embryos with magnified view and schematic cartoon with quantification of normalized mean intensity on the right. Embryos were injected with Membrane-RFP (magenta) and GFP-Cep104 (green, arrowhead and arrow). Scale bars represent 10 µm. (*n* = 80 cilia, 20 cells, 7 embryos, 3 experiments) Data are presented as mean values +/- SD. **I**–**L** Localization of distal proteins in control (**I**, **J**) and Ccdc78 MO injected (**K**, **L**) embryos with magnified view and schematic cartoon with quantification of normalized mean intensity on the right. Embryos were injected with Membrane-RFP (magenta) and GFP-Armc9 (green, arrow). Scale bars represent 10 µm. (*n* = 80 cilia, 20 cells, 7 embryos, 3 experiments) Data are presented as mean values +/- SD.

We quantified the local thickness of microtubule bundles inside clones expressing either protein and found them to be significantly increased compared to controls (Fig. 6D–F). Expression of Ccdc78 or Ccdc33 did not affect the total level of GFP-EMTB protein (Supplementary Fig. 8A, B) and uniform overexpression of either protein also caused marked bundling of microtubules (Supplementary Fig. 8C–E).

We then asked if these proteins could also bundle microtubules in vitro. We co-incubated fluorescently labeled, polymerized, and Taxol-

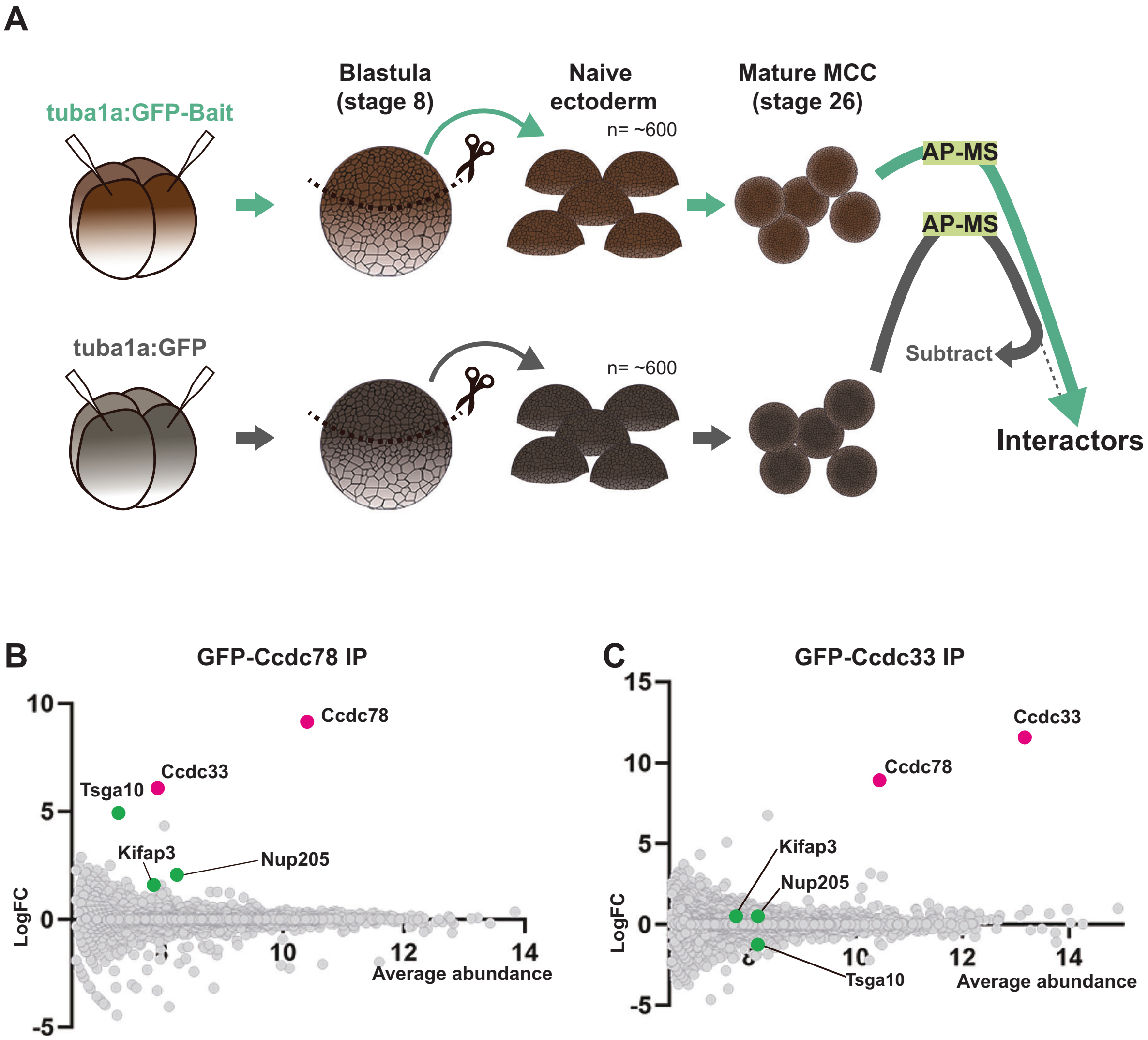

Fig. 3 | Ccdc78 interacts physically and functionally with Ccdc33 in the MCC cilia tip. A Workflow for AP-MS performed using *Xenopus* animal caps. (B-C) MA plot of log2 fold change and average abundance in comparison between GFP and GFP-Ccdc78 **B** or GFP-Ccdc33 **C** immunoprecipitation enriched proteins. Highly enriched proteins are labeled with magenta (Ccdc78 and Ccdc33) and green (Tsga10, Nup205, and Kifap3).

stabilized microtubules with in vitro translated GFP, GFP-Ccdc78, or GFP-Ccdc33. Microtubules incubated with GFP alone formed only sparse, small bundles (Fig. 6G). By contrast, the addition of either Ccdc78 or Ccdc33 resulted in the formation of prominent bundles throughout the sample (Fig. 6H, I). The increase in bundle thickness was significant (Fig. 6G′-I′).

Finally, we asked if the two proteins might function in concert. We found that the robust bundling achieved by 30 nM Ccdc78 or 20 nM Ccdc33 could also be achieved by 15 nM Ccdc78 together with 10 nM Ccdc33 (Fig. 6J, J′). These results demonstrate that Ccdc78 and Ccdc33 possess microtubule bundling activity in vivo and in vitro and support the idea that the two proteins work in concert to stabilize the distal tip of MCC motile cilia.

Ccdc78 and Ccdc33 control cilia length specifically in 9 + 2 motile cilia

Ccdc78 and Ccdc33 bundle microtubules and also control the localization of a coterie of additional proteins thought to stabilize the distal cilium, a region known to be important for ciliary length control[14,49,50]. Accordingly, we found that loss of either protein was sufficient to severely disrupt cilia length in MCCs. Ccdc78 KD severely reduced the length of MCC cilia by >8 microns (~57% of cilium length), a phenotype that was specific, since it was rescued by re-expression of Ccdc78 (Fig. 7A–D). Notably, this shortening of cilia length could not be explained merely by the loss of the distal cilium described above, as the Spef1-positive domain spans only ~2 microns (~15% of cilium length).

Ccdc33 KD also had a significant -if more modest- effect on cilia length, reducing it by ~6 microns; this effect was also specific since it was rescued by re-expression of Ccdc33 (Fig. 7E–H). Again, the loss of cilia length was too substantial to be explained only by the loss of the distal Spef1 domain.

Finally, because our localization data suggested that Ccdc78/33 acts as a cap on the central pair extension of 9 + 2 cilia, we asked if these proteins play any role in motile cilia that lack a central pair. We therefore examined 9 + 0 motile cilia in the *Xenopus* left/right organizer[51,52], where Ccdc78 was present at the base of cilia but absent at the tips as marked by Cep104 (Supplementary Fig. 9A). Ccdc33 was present at neither the base nor the tip of these cilia (Supplementary Fig. 9B). Moreover, KD of neither Ccdc78 nor Ccdc33 had any impact on the length of these motile 9 + 0 mono-cilia (Fig. 7I–L; Supplementary Fig. 9C–E). Thus, Ccdc78 and Ccdc33 play non-redundant roles in

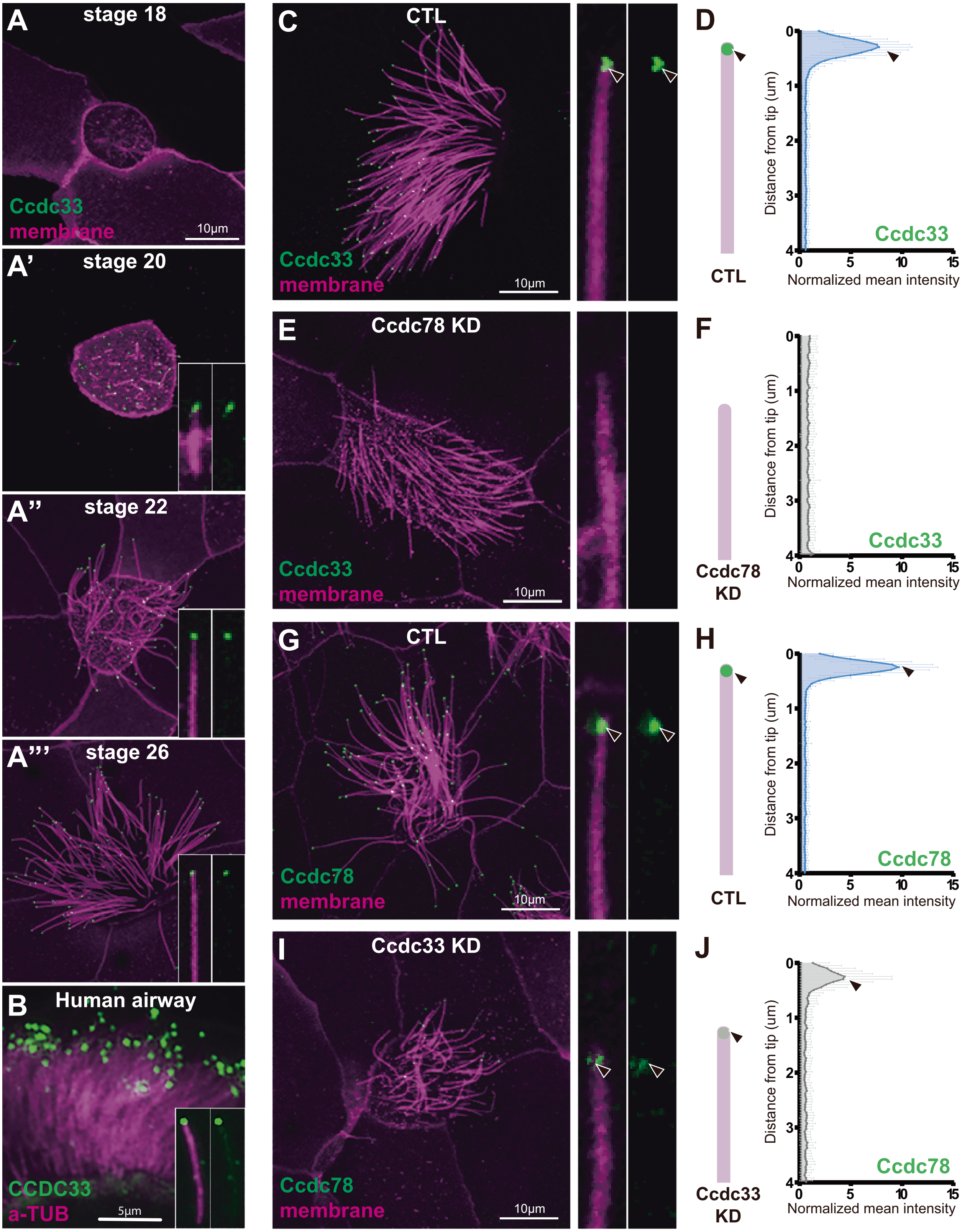

assuring normal cilia length specifically in the 9 + 2 motile cilia of vertebrate MCCs (Fig. 7M, N).

Ccdc78 and Ccdc33 control cilia length via distinct mechanisms

In our imaging data, it was apparent that while loss of either Ccdc78 or Ccdc33 reduced overall cilia length, the two phenotypes were quite distinct. After Ccdc78 KD, all cilia on each MCC were reduced in length to roughly the same degree. The loss was, on average, ~8 microns with a standard deviation of 1.6 (Fig. 7D). By contrast, Ccdc33 KD resulted in MCCs with heterogeneous cilia lengths. Their average length was reduced by ~6 microns, but the standard deviation was much higher, at a value of 2.2 (Fig. 7H).

We reasoned that this heterogeneous reduction in cilia length might be related to the partial loss of Ccdc78 that results from Ccdc33

Fig. 4 | Ccdc33 localizes to the extreme distal tip of MCC cilia interacting with Ccdc78 at the MCC cilia tip. A–A‴ Localization of GFP-Ccdc33 (green) with RFP-membrane (magenta) during ciliogenesis on *Xenopus* embryo epithelium. Magnified view of cilium on the bottom right. Scale bar represents 10 µm. **B** Human tracheal epithelial cell multi-cilia stained with anti-acetylated tubulin (magenta) and anti-CCDC33 (green) antibody. Scale bar represents 1 µm. **C**–**F** *Xenopus* MCC was injected with membrane-RFP (magenta) and GFP-Ccdc33 (green, arrowhead) in control (**C**, **D**) and Ccdc78 KD (**E**, **F**) embryo with magnified view and schematic cartoon with quantification of normalized mean intensity on the right. Scale bar represents 10 µm. ($n = 78$ cilia, 30 cells, 10 embryos, 3 experiments) Data are presented as mean values +/- SD. **G**, **H** *Xenopus* MCC injected with membrane-RFP (magenta) and GFP-Ccdc78 (green, arrowhead) in control (**G**, **H**) and Ccdc33 MO-injected (**I**, **J**) embryo with magnified view and schematic cartoon with quantification of normalized mean intensity on the right. Scale bar represents 10 µm. ($n = 78$ cilia, 30 cells, 10 embryos, 3 experiments) Data are presented as mean values +/- SD.

KD (see Fig. 4G–J, above). Consistent with this idea, we found that for any given Ccdc33 KD cilium, the intensity of Ccdc78-GFP at the tip correlated well with the length of that cilium (Fig. 8A–D). Moreover, a similar correlation was found between the length of the partial Spef1 domain and the length of the cilium (Fig. 8E–H).

These data prompted us to ask if overexpression of Ccdc78 might drive lengthening of cilia, but we observed no difference compared to controls (Fig. 8I–K). Expression of Ccdc78 likewise failed to rescue the loss of Ccdc33 (Fig. 8L–O). These data suggest that Ccdc33 elicits its effect on cilia length in part via its ability to recruit Ccdc78 to the tips of cilia and that an intact EDT is required for the normal length of the Spef1 domain and normal length of the cilium.

Finally, we considered that a possible explanation for the very distinct phenotypes elicited by loss of Ccdc78 and Ccdc33 may lie in the distinct structures of the proteins. While both are comprised of coiled-coils, Ccdc33 also has three lipid-binding C2 domains, which may drive its association with the ciliary membrane (Fig. 9A, B). These domains are crucial to Ccdc33 function, as their deletion completely abolished the ability of Ccdc33 to rescue the effects of Ccdc33 KD both in cilia length control and Spef1 localization (Fig. 9C, G).

Ccdc78 and Ccdc33 loss elicit distinct defects in cilia beating and fluid flow

The precise role of the cilia tip in cilia beating remains largely unresolved, as disruption of other cilia tip proteins is confounded by their possible roles outside the tip. Spef1, for example, is dramatically enriched distally but is also present along the entire length of the axoneme, and Spef1 mutant cilia entirely lack the central pair[9,25]. Likewise, Eb1 and Eb3 bind the minus ends of cytoplasmic microtubules[21,22], and Cep104 is present at basal bodies as well as cilia tips[13]. Ccdc78 and especially Ccdc33, therefore, provide entry points for examining the functional consequences of disrupting the cilia tip. Notably, the two knockdowns elicited strikingly different beating phenotypes.

In spinning disk confocal microscopy, the metachronal wave of beating cilia was expectedly normal in control MCCs. To our surprise, metachrony also appeared normal after Ccdc78 KD (Fig. 10A, B; Supplementary Movies 1, 2). While the uniform reduction of cilia length was apparent in our videos, demonstrating that knockdown was effective in the samples, we nonetheless observed no qualitative defect in their beating (Fig. 10B, Supplementary Movie 2). By contrast, beating was visibly defective after Ccdc33 KD. In some cells, cilia appeared stiffer and metachrony was entirely absent (Fig. 10C, Supplementary Movie 3). In other cells, metachrony was observed in patches where cilia length was more uniform but was absent from other regions of the same cell (Fig. 10D, Supplementary Movie 4).

Because Ccdc78 and Ccdc33 control Spef1 localization at the tips of cilia, and Spef1 is also present at the planar polarized ciliary rootlet[53], we considered the possibility that defects at the rootlet might underlie the cilia beating defects. However, Spef1 was normally localized adjacent to basal bodies in controls as well as in Ccdc78 or Ccdc33 KD (Supplementary Fig. 10E–G). Consistent with the normal metachrony, rootlets were planar polarized in controls and Ccdc78 KD (Supplementary Fig. 10E, F). Normal beating is required to entrain planar polarity[54] and we accordingly observed the expected disruption of rotational polarity after Ccdc33 KD (Supplementary Fig. 10G).

The distinct beating patterns then prompted us to assess fluid flow, the functional output of MCC cilia beating. To this end, we imaged fluorescent tracer bead movement across the *Xenopus* embryo medium using spinning disk confocal microscopy. We visualized flow using Flowtrace[55] and quantified the data using Particle Imaging Velocimetry[56]. This analysis revealed the expected highly aligned fluid flow near the embryo surface with less robust but still obvious flow in regions farther from the surface (Fig. 10E, E′, Supplementary Movie 5). Consistent with the relatively normal metachronal beating, Flowtrace revealed that flow was aligned and coordinated near the surface after Ccdc78 KD, though flow speed was strongly reduced and the coordination of flow decayed quickly with distance from the surface (Fig. 10F, F′, Supplementary Movie 6). By contrast, we observed a near-total absence of coordinated flow in Ccdc33 KD embryos (Fig. 10G, G′, Supplementary Movie 7). These patterns were highly consistent across samples (Fig. 9H).

To quantify this effect, we calculated flow in two regions separated at the point of maximum decline in speed (Supplementary Fig. 10A–D). Within the region near the surface, Ccdc78 KD reduced flow speed by roughly 50%, while Ccdc33 KD reduced speed by ~90% (Fig. 10I, adjacent). In the region farther from the surface, the modest flow observed for controls was effectively eliminated by the loss of either protein (Fig. 10I, far). These data link the disruption of the EDT and the overall organization of the cilia tip to defects in cilia beating and cilia-mediated fluid flow.

Discussion

We have defined a domain in the extreme distal tip of vertebrate MCC cilia that is defined by the presence of Ccdc78 and Ccdc33 (Fig. 1). These proteins function non-redundantly and are required for normal localization of several additional ciliary tip proteins (Figs. 2–5). Ccdc78 and Ccdc33 display robust microtubule bundling activity both in vivo and in vitro (Fig. 6). Moreover, both proteins – and by extension the EDT itself – are necessary for maintaining normal ciliary length control in MCCs (Figs. 7, 8). Finally, both are likewise required for cilia beating for MCC's ability to generate normal fluid flows across the epithelium (Fig. 10). These data provide a depth of understanding of the molecular architecture of MCC cilia tips and should be significant on several levels.

First, our data allow us to propose a model whereby Ccdc78 and Ccdc33 non-redundantly stabilize microtubules via their bundling activity. Since Ccdc78 is entirely necessary for Ccdc33 localization to the ciliary tip, we suggest that after Ccdc78 KD, the loss of both proteins from the tip leads to the observed uniform, severe length defect. By contrast, Ccdc33 KD elicits only a partial loss of Ccdc78 localization to the tip, which leads to the heterogeneous reduction of cilia length. And the heterogeneity of cilia length may result in more severe cilia length-dependent phenotypes.

Neither length phenotype can be explained simply by loss of the central pair extension (i.e., that marked by Spef1), so our data suggest two possibilities. First, axonemes may be destabilized in the absence of microtubule bundling by Ccdc78/33 and shortened by disassembly as a consequence of the forces associated with ciliary beating. Indeed, the

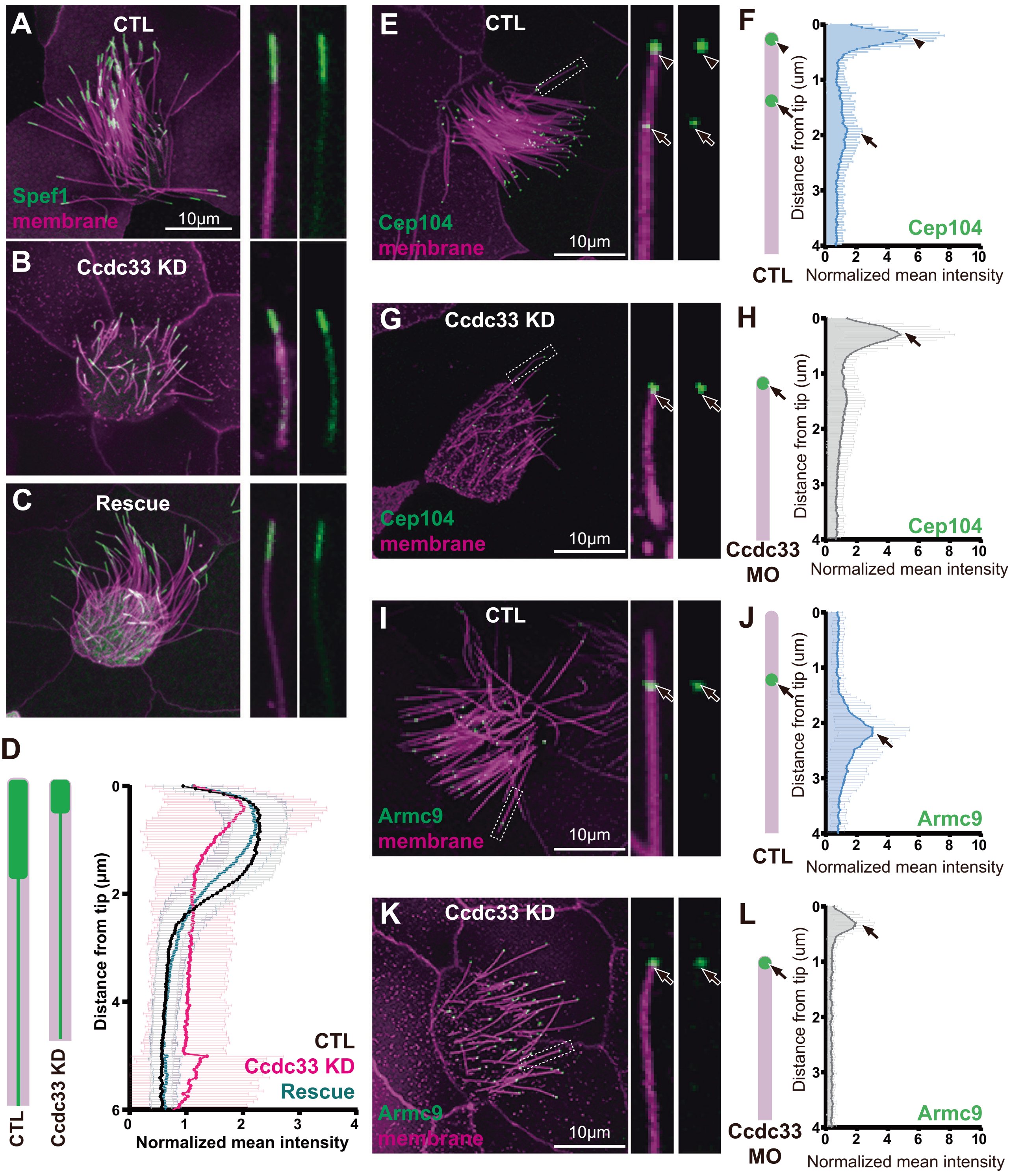

Fig. 5 | Ccdc33 is required for localization of distal tip proteins in MCC. **A–C** Image of GFP-Spef1 (green) and membrane-RFP (magenta) injected *Xenopus* multi-cilia in control **A**, Ccdc33 MO-injected **B**, and rescued **C** embryos. Scale bars represent 10 μm. **D** Schematic cartoon of Spef1 distribution in control and Ccdc33 MO-injected cilium. Quantification of fluorescent intensity of GFP-Spef1 along the axoneme normalized by average intensity in control, Ccdc33 MO-injected and rescued embryos. (*n* = 65 cilia) Data are presented as mean values +/- SD. **E–H** Localization of distal proteins in control (**E**, **F**) and Ccdc33 MO-injected (**G**, **H**) embryos, with magnified view and schematic cartoon with quantification of normalized mean intensity on the right. Embryos were injected with membrane-RFP (magenta) and GFP-Cep104 (green, arrowhead and arrow). Scale bars represent 10 μm. (*n* = 180 cilia, 36 cells, 12 embryos, 3 experiments) Data are presented as mean values +/- SD. **I–L** Localization of distal proteins in control (**I**, **J**) and Ccdc33 MO-injected (**K**, **L**) embryo with magnified view and schematic cartoon with quantification of normalized mean intensity on the right. Embryos were injected with membrane-RFP (magenta) and GFP-Armc9 (green, arrow). Scale bars represent 10 μm. (*n* = 85 cilia, 27 cells, 9 embryos, 3 experiments) Data are presented as mean values +/- SD.

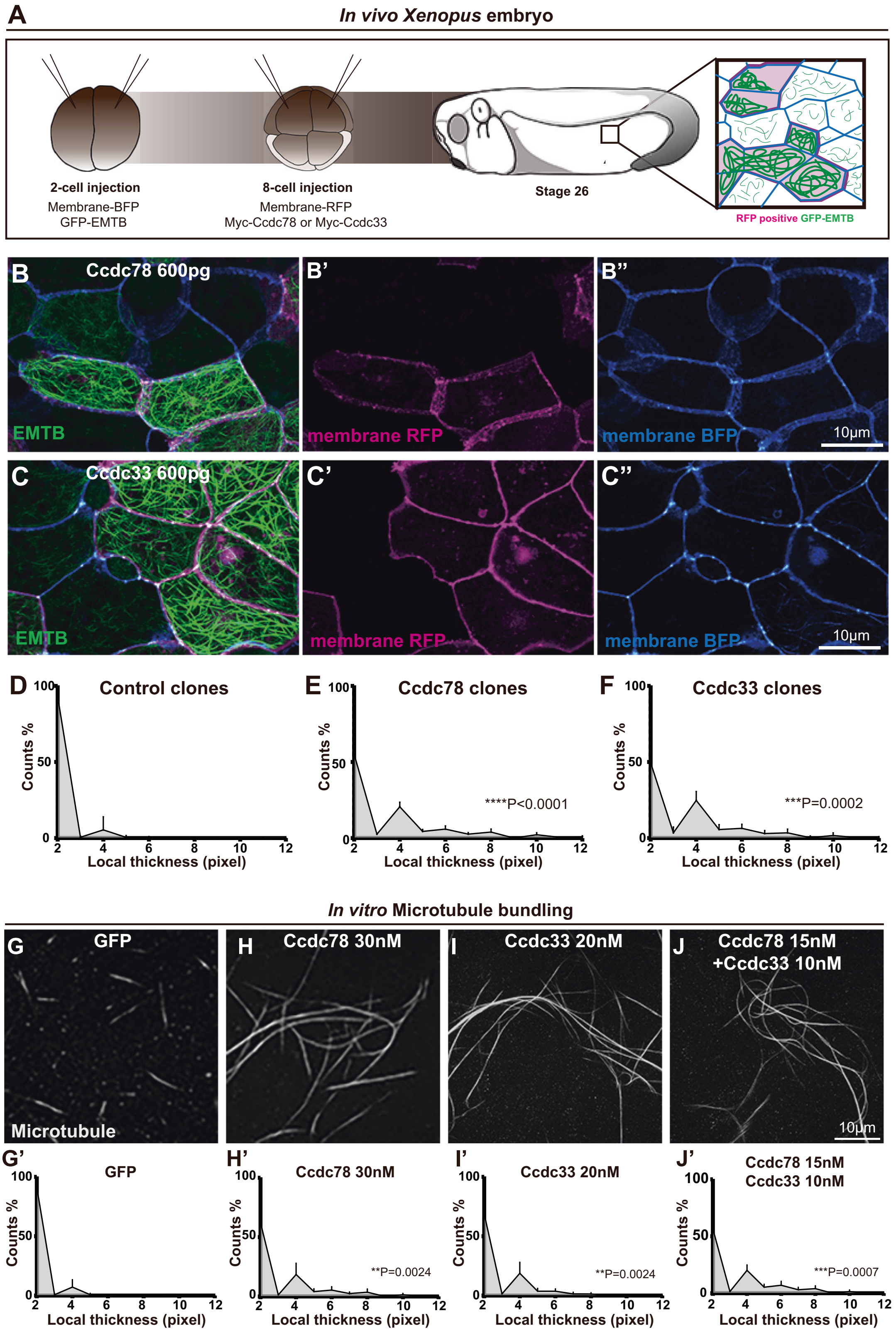

whip-like movement of cilia increases mixing and velocity of the surrounding fluid most strongly near ciliary tips[44,45], suggesting the distal axoneme is subjected to higher mechanical stress. In this light, it is notable that like Ccdc78/33, Spef1 also displays robust MT bundling and stabilizing activity in vivo and in vitro, and that MT bundling activity is necessary for Spef1 to support ciliary beating[25,43,57]. Alternatively, since elongation of the axoneme is controlled at the tip, Ccdc78/33 may somehow control the elongation machinery directly, for example via IFT turnaround[58–60]. Consistent with this notion, we identify the IFT kinesin subunit Kif3ap as a Ccdc78 interactor.

In addition, we found that Ccdc78 and Ccdc33 are present at the distal ends of *Xenopus* as well as mammalian tracheal and oviduct MCCs. This evolutionary conservation is likely very ancient because vertebrate Ccdc33 comprises coiled-coil regions and lipid-binding C2

Fig. 6 | Ccdc78 and Ccdc33 display microtubule bundling activity in vivo and in vitro. A Workflow for generating mosaic expression in *Xenopus* embryo. **B**, **C** Image of *Xenopus* embryo goblet cells on epithelium expressing GFP-EMTB (green), membrane-BFP (blue), and membrane-RFP(magenta) in embryos injected with Myc-Ccdc78 600 pg (**B**–**B″**) and Myc-Ccdc33 600 pg (**C**–**C″**). Cells expressing membrane-RFP correspond to those overexpressing Myc-ccdc78 or Myc-ccdc33, indicating mosaic expression. Scale bars represent 10 µm. **D**–**F** Quantification of local thickness ($n = 26$, 13 embryos across 3 experiments). The distribution of local thickness was compared between control **D** and Ccdc78 600 pg **E** or Ccdc33 600 pg **F** using two-sided Kolmogorov-Smirnov test (KS-test), the KS-distance and *P*-value are shown on right. CTL vs Ccdc78 600 pg $****p < 0.0001$, CTL vs Ccdc33 600 pg $***p = 0.0002$. Data are presented as mean values +/- SD. **G**–**J** Image of 647-fluorophore labeled microtubules (gray) incubated with GFP **G**, GFP-Ccdc78 30 nM **H**, GFP-Ccdc33 20 nM **I** and GFP-Ccdc78 15 nM with GFP-Ccdc33 10 nM **J**. Scale bar represents 10 µm. **G′**–**J′** Quantification of local thickness($n = 15$ across 2 experiments). The distribution of local thickness was compared between control (**G′**) and Ccdc78 30 nM (H′) or Ccdc33 10 nM (**I′**) or GFP-Ccdc78 15 nM with GFP-Ccdc33 10 nM (J′) using two-sided Kolmogorov-Smirnov test (KS-test), the KS-distance and P-value are shown in right. GFP vs GFP-Ccdc78 30 nM $**p = 0.0024$, CTL vs GFP-Ccdc33 20 nM $**p = 0.0024$, GFP vs GFP-Ccdc78 15 nM & GFP-Ccdc33 10 nM $***p = 0.0007$. Data are presented as mean values +/- SD.

domains, suggesting it is a direct orthologue of the C2D1 protein reported with a similar structure at the distal ends of *Tetrahymena* cilia[9,10] (Supplementary Fig. 11A–C). Likewise, a protein with homology to Ccdc78 has also been found at the distal tip of *Tetrahymena* cilia (Uniprot: I7LVY1)[10], though that protein is characterized by a kinesin motor domain that is absent from vertebrate Ccdc78 (Supplementary Fig. 11D–F). Our data also reveal that Spef1, Cep104, and Armc9 in the distal tips of *Xenopus* MCC cilia all display similar patterns to that observed in *Tetrahymena*[9–11].

These similar patterns of protein localization are of interest because they suggest that the molecular architecture underlying 9 + 2 distal tips is deeply conserved, despite the fact that the ultra-structures of these regions are highly variable across species, across cell type, and even across developmental stage for a single cell type. Indeed, older EM studies suggest that a “cap” structure connects microtubules at the tip to the ciliary membrane in a wide range of vertebrate MCCs[7,17]. Since Ccdc33 contains lipid-binding C2 domains[61], Ccdc33 and Ccdc78 may be essential components of these cap structures.

Finally, our data provide insights into the relationships between the tip, cilia length, metachrony, and fluid flow. We find that the uniform decrease in length of cilia after Ccdc78 loss allows normal metachronal beating but results in reduced overall fluid flow speeds (Fig. 10). This is consistent with the theory suggesting that shorter cilia produce less flow[62]. More interesting are the beating defects after Ccdc33 KD. It is possible these stem directly from Ccdc33 function at the tip, but this seems unlikely because beating and metachrony are largely normal after Ccdc78 KD, yet Ccdc33 is entirely lost from the tip (Fig. 4). Another possibility is that the reduced cilia length coupled to length heterogeneity disrupts metachrony and thus severely disrupts flow even adjacent to the epithelium (Fig. 10). This interpretation is reasonable, as metachrony arises from hydrodynamic coupling[63–65] and in theoretical models is sensitive to noise in the system[66,67].

In light of their roles in cilia beating, it is notable that neither *CCDC78* nor *CCDC33* has previously been associated with motile ciliopathy. Rather, *CCDC78* is implicated in myopathy[68]. Not all studies support this association, however[69], and both bulk and single-cell RNAseq in the Human Protein Atlas demonstrate that human *CCDC78* is strongly expressed in tissues that contain MCCs and at only very low levels in all other tissues, including muscle[70,71]. On the other hand, one report implicates *CCDC78* in myopathy associated with respiratory insufficiency[72], which would be consistent with a defect in cilia beating. If *CCDC78* variants do contribute to myopathy, the effect may relate to the protein’s association with centrioles in MCCs, as CCDC78 was found to localize to centrosomes in HeLa cells[73]. *CCDC33* is not yet associated with any disease, but it is enriched only in tissues that contain MCCs and is co-expressed with *CCDC78* in an MCC-related cluster in scRNAseq data[70,71].

Given that many cases of human ciliary dyskinesia go undiagnosed and that many, too, are associated with grossly normal ultrastructure of the beating machinery such as dynein arms, radial spokes, or the central pair[74,75], our data suggest that EDT defects may explain failure of cilia beating in certain patients. As such, *CCDC78* and especially *CCDC33* represent interesting candidate loci for human motile ciliopathy.

Methods

Animal husbandry and embryo manipulation

All *Xenopus* experiments were conducted in accordance with the animal protocol AUP-2024-00130 and the animal ethics guidelines of the University of Texas at Austin. To induce ovulation, female adult *Xenopus laevis* was injected with 400 units of hCG (Human chorionic gonadotropin) and incubated in a 16 °C incubator for overnight. In vitro fertilization was performed by mixing the *Xenopus egg* with homogenized testis in 1/3X MMR (Marc’s Modified Ringer’s). Fertilized embryos were then de-jellied with 3% L-cysteine in 1/3X MMR (pH 7.8), washed, and manipulated in 1/3X MMR.

All mice experimental procedures received approval from the Animal Care and Use Committee of Nagoya City University and were conducted in accordance with the Institutional Guidelines for Animal Experimentation (Approval Number: 23-001H05).

Plasmids, mRNA and Morpholino

Gene sequence for *Xenopus laevis* was obtained from Xenbase (https://www.xenbase.org/). Total RNA was purified from *Xenopus laevis* embryo and then reverse transcribed into cDNA library using M-MLV Reverse Transcriptase (Invitrogen). Coding sequence (CDS) of genes was amplified from the *Xenopus* cDNA library by PCR (Polymerase chain reaction) using Q5® High-Fidelity DNA Polymerase (NEB). Primer pairs were designed with restriction enzyme sites for cloning. Amplified genes and the pCS10R vector containing a fluorescence tag were digested with restriction enzymes, ligated together, and inserted into competent cells by transformation. Cloned constructs were linearized to synthesize mRNA using mMESSAGE mMACHINE™ SP6 Transcription Kit (Invitrogen). The list of cloned genes is as follows: Armc9, Cep104, Ccdc78, Ccdc33, Spef1, Spag6, Cfap52, Ak7, Tsga10, EMTB.

Anti-sense morpholinos were designed to block RNA splicing based on the sequence from Xenbase database. The morpholinos were manufactured by Gene Tools. Ccdc78 and Ccdc33 morpholino sequences are as follows:

Ccdc78.L MO: 5′-CCCATTCCTTTCACTTACATTTTC-3′
Ccdc33.L MO: 5′-GGTCAGGTAGTCACAGTATAAGAA-3′

Embryo microinjection and sample preparation

Embryo microinjection was done in 2% ficoll in 1/3X MMR. For the multi-ciliated cell visualization, 2-cells of ventral-animal side in 4-cell stage embryos were injected with fluorescence tagged mRNA (<80 pg/cell for localization, 600 pg/cell for overexpression) and morpholinos. For the nodal cilia visualization, two dorsal-ventral cells in 4-cell stage embryos were injected with GFP-tagged Arl13b, BFP-tagged cent4 and mScarlet3-tagged Ccdc78 or Ccdc33.

For multi-ciliated cells live-imaging, *Xenopus* embryos were incubated until stage 26 after microinjection. Whole embryos were mounted between the cover glass with a small amount of 1/3X MMR and imaged immediately. For nodal cilia live-imaging, *Xenopus* embryos were incubated until stage 18 after the microinjection.

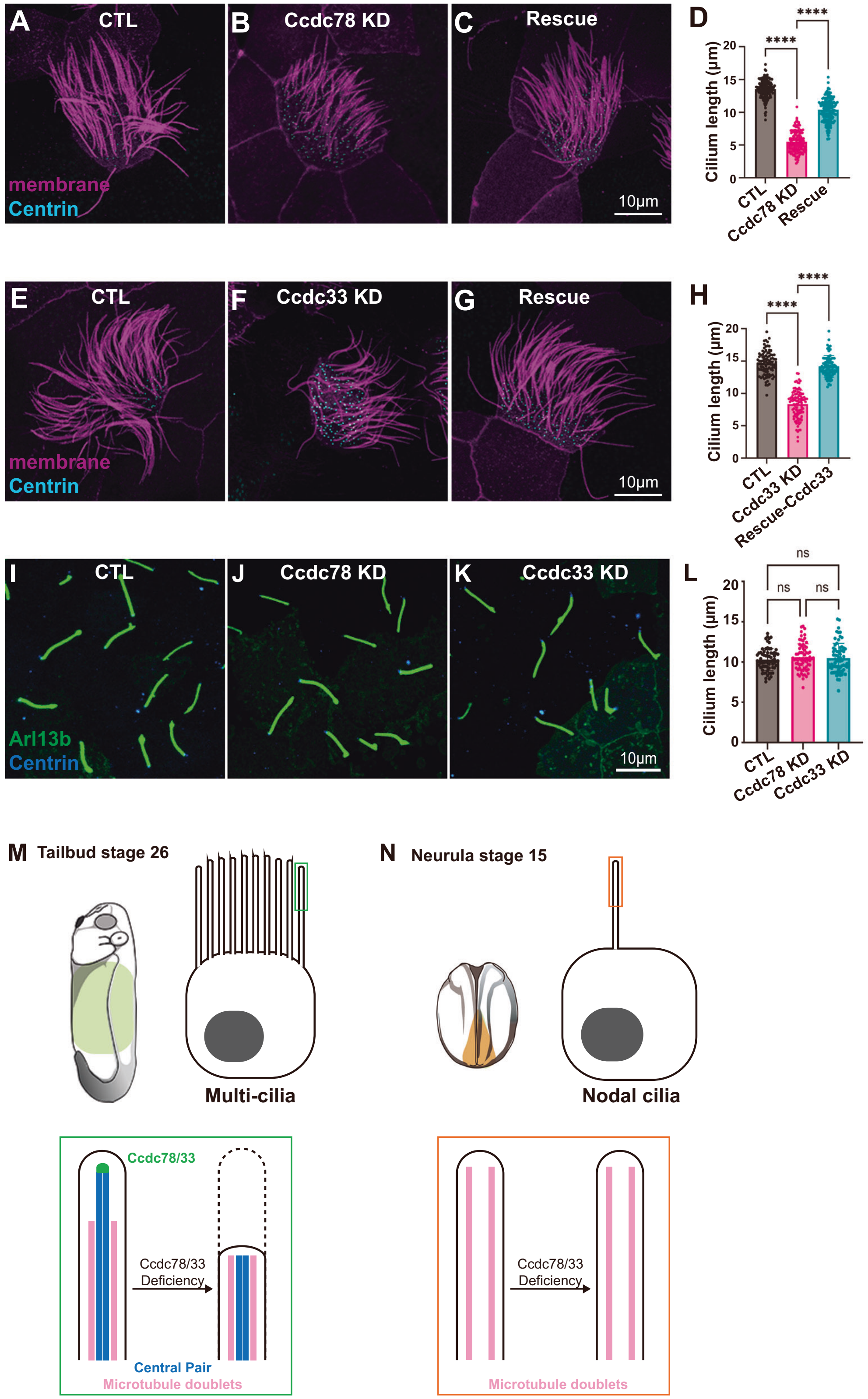

Embryos were dissected laterally to the dorsal posterior to obtain the gastrocoel roof plate (GRP) region. Dissected explants were mounted in the same way as whole embryos and imaged immediately.

Image acquisition and analysis

Confocal images were acquired with Zeiss LSM700 laser scanning confocal microscope using a plan-apochromat 63X/1.4 NA oil objective lens (Zeiss). Structured illumination microscopy (SIM) images were acquired with Nikon DeepSIM microscopy using a 100X oil objective lens (Nikon).

Quantitative measurement of images was done using Fiji. The fluorescent intensity values of each measured pixel for each protein were normalized with the average intensity of the entire distal-most four microns of individual cilia. Graph generation and statistical

Fig. 7 | Ccdc78 and Ccdc33 are essential for length control specifically in 9 + 2 motile cilia. A–**C** *Xenopus* MCC injected with membrane-RFP (magenta) and Centrin-BFP (cyan) in control **A**, Ccdc78 MO **B** and rescued **C** embryos. Scale bar represents 10 μm. **D** Quantification of the length of cilium. ****$p < 0.0001$. ($n = 147$ cilia, 36 cells, 12 embryos across 3 experiments) (Ordinary one-way ANOVA) Data are presented as mean values +/- SD. **E**–**G** *Xenopus* MCC injected with membrane-RFP (magenta) and Centrin-BFP (cyan) in control **E**, Ccdc33 MO **F** and rescued **G** embryos. Scale bar represents 10 μm. **H** Quantification of the length of cilium is shown. ****$p < 0.0001$. ($n = 100$ cilia, 30 cells, 10 embryos across 3 experiments) (Ordinary one-way ANOVA) Data are presented as mean values +/- SD. **I**–**K** Image of *Xenopus* gastrocoel roof plate 9 + 0 motile cilia injected with GFP-Arl13b (green) and Centrin-BFP (blue) in control **I**, Ccdc78 KD **J** and Ccdc33 KD **K** embryos. Scale bar represents 50 μm. Magnified view of images are shown in right with 10 μm scale bar. **L** Quantification of the length of cilia. ($n = 68$ cilia, 8 embryos across 3 experiments) (Ordinary one-way ANOVA) Data are presented as mean values +/- SD. **M**, **N** Schematic images of *Xenopus* embryo at tailbud stage **M** and neurula stage **N**. The MCC 9+2 cilia are composed of microtubule doublets and a central pair, where the extreme distal tip of the central pair is labeled with Ccdc78/33. Loss of Ccdc78/33 results in disruption of distal ciliary region in MCC. On the other hand, nodal 9 + 0 cilia are composed of microtubule doublets only. Ccdc78/33 is not present in nodal cilia tip, thereby the 9 + 0 motile cilia are not affected by Ccdc78/33 deficiency.

analysis including error bars, mea*n* ± SD and *P* values were performed using Prism 10 software.

Cilia isolation and negative staining for TEM

Xenopus embryos in tailbud stage were anesthetized with 0.05% Benzocaine in 1/3X MMR and washed with 1/3X MMR several times to clear the debris from vitelline envelope and excess mucus. Embryos were transferred to the 2 ml PCR tube and incubated with deciliation buffer (20 mM HEPES pH 7.0, 112 mM NaCl, 3.4 mM KCl, 10 mM CaCl2, 2.4 mM $NaHCO_3$, 20% EtOH, 1x protease cocktail) for 45 seconds on a nutator. The supernatant with isolated cilia was transferred to another 2 ml PCR tube and centrifuged for 5 min at 13,000 x *g*. The pellet was resuspended and fixed with 0.15% Glutaraldehyde for 10 minutes in room temperature. After centrifugation for 5 minutes at 13,000 x *g*, the cilia pellet was resuspended and washed with 1X PBS, then centrifuged again for 5 minutes at 13,000 x *g*. The final cilia pellet was resuspended with 20 μl of 1X PBS.

For negative staining, 5 μl of isolated cilia was placed on the grid (Formvar/Carbon 300 Mesh, Cu, Electron microscopy sciences) and sat for 1 min. The grid was stained with 2% uranyl acetate solution and washed with water. Air-dried grids were stored in the grid box for further imaging. The imaging of samples was done with JEOL NEOARM Low kV STEM.

Protein purification and Immunoprecipitation

GFP-tagged Ccdc78 and Ccdc33 plasmids, respectively, were injected into 2-cell embryos of the ventral-animal side of the *Xenopus* embryos at the 4-cell stage. Injected embryos were incubated until they reached stage 9, and their animal caps were dissected in Steinberg's solution with gentamicin. When animal caps reached stage 26, they were collected for protein extraction.

Protein purification and immunoprecipitation were performed with the GFP-Trap agarose kit (Chromotek). Collected embryos were lysed with lysis buffer containing 1X protease inhibitor (Thermo Scientific™ Halt™ Protease Inhibitor Cocktail (100X), Thermofisher) and 1 mM PMSF (Phenylmethylsulfonyl fluoride). Lysed samples were centrifuged in 4°C for 15 min with 14,000 rpm to separate the lipid layer and collect clear lysates. GFP-agarose beads were equilibrated in dilution buffer according to the manufacturer's protocol. GFP-agarose beads in dilution buffer were added to the lysate and incubated at 4°C for 1 hour. After protein binding, beads were centrifuged at 4°C for 5 minutes at 2500xg. Pelleted beads were washed with wash buffer 2 times and added in 1.5X Laemmli sample buffer with 5% (v/v) 2-Mercaptoethanol. After boiling at 95°C, beads were pelleted with 4°C centrifuge for 5 minutes and the supernatant was collected and stored at -80°C for further analysis.

Affinity purification mass spectrometry

Immunoprecipitated proteins were resuspended in SDS-PAGE sample buffer and heated for 5 min at 95 °C before loading onto a 7.5% acrylamide mini-Protean TGX gel (BioRad). After 7 min of electrophoresis at 100 V, the gel was stained with Imperial Protein stain (Thermo) according to the manufacturer's instructions. The protein band was excised, diced to 1 mm cubes and processed for in-gel trypsin digestion as in Goodman et al., 2018[76]. Digested peptides were desalted with 6μg-capacity ZipTips (Thermo Scientific), dried, and resuspended in 20 μl of 5% acetonitrile, 0.1% acetic acid for mass-spectrometry. Peptides were separated using reverse phase chromatography on a Dionex Ultimate 3000 RSLCnano UHPLC system (Thermo Scientific) with a C18trap to EASY-Spray PepMap RSLC C18 column (Thermo Scientific, ES902) configuration eluted with a 3% to 45% gradient over 60 min. Spectra were collected on a Thermo Orbitrap Fusion Lumos Tribrid mass spectrometer using a data-dependent top speed HCD acquisition method with full precursor ion scans (MS1) collected at 120,000 m/z resolution. Monoisotopic precursor selection and charge-state screening were enabled using Advanced Peak Determination (APD), with ions of charge + two selected for high energy-induced dissociation (HCD) with stepped collision energy of 30% +/- 3% (Lumos). Dynamic exclusion was active for ions selected once with an exclusion period of 20 s (Lumos). All MS2 scans were centroid and collected in rapid mode. Raw MS/MS spectra were processed using Proteome Discoverer (v2.5) and the Percolator node to assign unique peptide spectral matches (PSMs) and protein assignments (FDR.01) to a *X. laevis* proteome derived from the 2023 UniProt *Xenopus laevis* reference proteome of 35,860 protein sequences with homeologs and highly related entries collapsed into EggNOG vertebrate-level orthology groups[77].

In order to identify proteins significantly associated with each bait, we used the degust statistical framework (https://degust.erc.monash.edu/) to calculate both a log2 fold-change and an FDR for each protein enrichment based on the observed PSMs in the bait versus control pulldown. Settings used were "RUV (edgeR-quasi-likelihood), Normalization TMM, and Flavour RUVr" and at least 2 counts in at least 2 samples.

RT-PCR

To confirm the efficacy of Ccdc78 and Ccdc33 morpholinos, morpholinos were injected into all cells at the 4-cell stage of embryos. Total RNA was isolated with Trizol reagent at stage 26, and cDNA was synthesized with M-MLV reverse transcription kit (Invitrogen). *ccdc78*, *ccdc33* and *odc1* were amplified by Taq-polymerase (Invitrogen) with the primers as follows:

ccdc78 Forward: 5′-AGAAGATCGTGAGACCCCCC-3′
ccdc78 Backward: 5′-TCAAGCTCTGCTGTGGCTTC-3′
ccdc33 Forward: 5′-GCTTCCAGAACAACACCTACCTTT-3′
ccdc33 Backward: 5′-GTGAGACAGGCGGAGAATCATCTA-3′

Immunoblotting

Xenopus laevis embryos were injected with GFP-Ccdc78 or GFP-Ccdc33 in all cells at the 4-cell stage with Ccdc33 or Ccdc78 morpholino, respectively. At stage 26, embryos were lysed in lysis buffer containing 1X protease inhibitor (Thermo Scientific™ Halt™ Protease Inhibitor Cocktail (100X), Thermofisher) and 1 mM PMSF (Phenylmethylsulfonyl fluoride). Fat was removed by centrifuging the samples with 12000xg

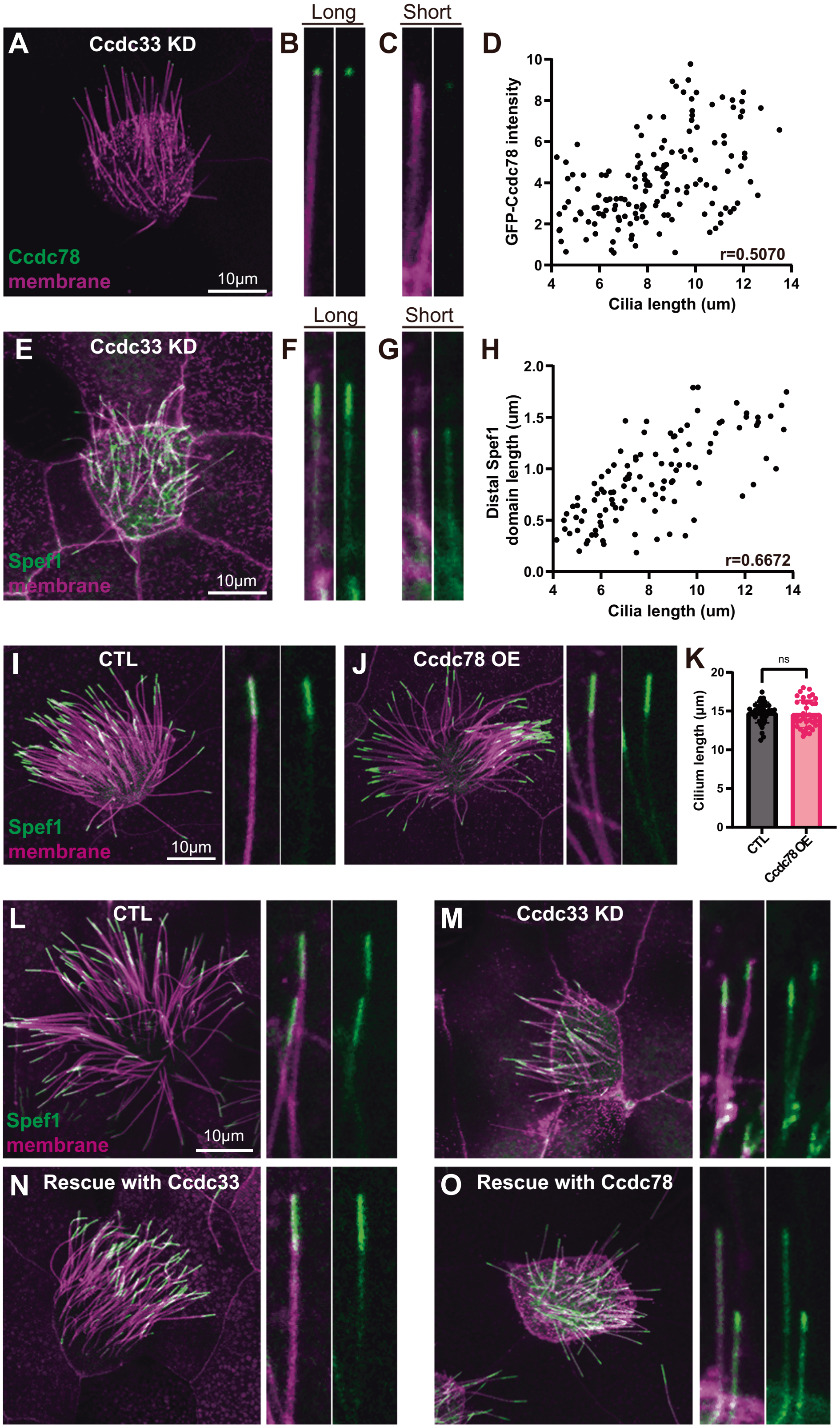

at 4 °C for 15 minutes. The clear lysate was added with 4X Laemmli sample buffer with 5% (v/v) 2-Mercaptoethanol and heated to 95 °C for 10 min. Protein samples were loaded on SDS-PAGE and transferred to nitrocellulose membranes. The membrane was incubated in blocking solution (0.05% Tween-20 in TBS with non-fat powdered milk) at room temperature for 30 minutes. For immunoblotting, membranes were sealed with mouse anti-beta-actin (1:10000, 66009-1, Proteintech), mouse anti-GFP (1:1000, sc-9996, Santacruz Biotechnology) or mouse anti-Myc (1:1000, 9E10, abcam) in 1% BSA solution for 1 hour at room temperature. Secondary labeling was performed using anti-mouse IgG HRP-conjugated (1:2000, 31430, ThermoFisher Scientific) secondary antibodies for 1 h at room temperature. Chemiluminescence was performed with enhanced chemiluminescence substrate and imaged with Image Quant (LAS 4000, GE Healthcare).

Fig. 8 | Deficiency of Ccdc33 shows heterogeneous MCC cilia phenotype. **A**–**C** Confocal image of *Xenopus* MCC injected with membrane-RFP (magenta) and GFP-Ccdc78 (green) in Ccdc33 KD embryos. The magnified view of relatively longer **B** or shorter **C** cilium are shown on the right. Scale bar represents 10 µm. **D** Correlation between cilia length and GFP-Ccdc78 intensity at the ciliary tip in Ccdc33 KD embryos MCCs. Each dot represents a single cilium. A moderate positive correlation was observed (Pearson's correlation coefficient, r = 0.5070). **E**–**G** Confocal image of *Xenopus* MCC injected with membrane-BFP (magenta) and Spef1-RFP (green) in Ccdc33 KD embryos. The magnified view of relatively longer **F** or shorter **G** cilium are shown on the right. Scale bar represents 10 µm. (*n* = 150 cilia, 37 cells, 13 embryos across 3 experiments). **H** Correlation between cilia length and Spef1-RFP intensity at the ciliary tip in Ccdc33 KD embryos MCCs. Each dot represents a single cilium. A moderate positive correlation was observed (Pearson's correlation coefficient, r = 0.6672). (*n* = 123 cilia, 32 cells, 11 embryos across 3 experiments). **I** Confocal image of GFP-Spef1 and membrane-RFP labeled in control MCC with magnified view of cilia on the right. Scale bar represents 10 µm. **J** Confocal image of GFP-Spef1 and membrane-RFP labeled in MCC overexpressed with 700 pg of *ccdc78* mRNA, magnified view of cilia on the right. Scale bar represents 10 µm. **K** Quantification of the length of cilium comparing between control and Ccdc78-overexpressed MCC. *p* = 0.6268 (*n* = 68 cilia, 20 cells, 9 embryos across 3 experiments) (Unpaired t-test) Data are presented as mean values +/- SD. (L-O) Image of *Xenopus* MCC labeled with GFP-Spef1 and membrane-RFP in control **L**, Ccdc33 Knockdown **M**, rescue with 600 pg of *ccdc33* mRNA **N** and rescue with 600 pg of *ccdc78* mRNA **O**, with magnified view of cilium on the right. Scale bar represents 10 µm.

C57BL/6JmsSlc mice were procured from Japan SLC, Inc. The mice were maintained under a 12-h light/dark cycle with free access to food and water. All experimental procedures received approval from the Animal Care and Use Committee of Nagoya City University and were conducted in accordance with the Institutional Guidelines for Animal Experimentation (Approval Number: 23-001H05). The trachea tissues from P10 (postnatal day 10) or P50 mouse were sonicated in SDS sample buffer and centrifuged for 1 h at 14,000 rpm. The boiled supernatant samples were separated by SDS-PAGE and blotted to a PVDF membrane. The membrane was blocked with 2% skim milk in PBS, and probed with anti-CCDC78 (1:1000, 26876-1-AP, Proteintech) or anti-beta-actin (1:2000, A5441, Sigma) antibodies. The antibody for CCDC78 was diluted in Can Get Signal solution 1 (NKB-201, Toyobo). After washing, the membrane was incubated with HRP-conjugated secondary antibodies, and visualized with ECL (WBKLS0500, Millipore).

Human cells immunoblot analysis was performed as previously described with minor modification as follows[78]. Cells were lysed in radioimmunoprecipitation assay (RIPA) buffer (Pierce, cat no. 89900) for 45 min at 4 °C. Lysates (45 µg) were separated by SDS-PAGE on NuPage 4–12% gels (Bis-Tris Gel; Invitrogen, cat no. NP0335BOX), transferred to polyvinylidene fluoride membranes and blocked in 5% (w/v) milk powder in TBS-T buffer (0.2% Tween-20 in TBS), for 1 h at room temperature. Membranes were incubated with Mouse anti-human CCDC33 (1:500, sc-390852, Santa Cruz), Rabbit anti-CCDC78 (1:500, 26876-1-AP, Proteintech) or Mouse anti-actin (1:2000, MAB1501R, Millipore Sigma) for up to 72 h, at 4 °C, washed three times for 30 min each then incubated in rabbit or mouse horseradish peroxidase-conjugated secondary antibodies (1:5000, 31460 or 31430, Invitrogen), diluted 1:5,000, for 1 h at room temperature. Antibodies were visualized using Pierce ECL western blotting substrate (Thermo Fisher Scientific, #32106) and the signal was detected on X-ray film.

Human ALI culture and immunostaining

Human trachea epithelial cells (HTECs) culture was prepared from airway epithelial cells isolated from tracheobronchial tissues as previously described[79]. Use of human tissues was reviewed by the Washington University Institutional Review Board. Anonymized human tissues were obtained from surgical excesses of deceased individuals and experimented by Code of Federal Regulations, 45 CFR Part 46, as not meeting criteria for human subject research. Briefly, epithelial cells were isolated from the tissues following incubation in pronase and differential adhesion on tissue culture plates. Basal cells were expanded in custom media, then released by trypsin treatment and cultured on Trans-well membranes (Trans-well, Corning, 3460). Cells were differentiated using air-liquid interface (ALI) conditions and media previously described[79,80].

Cultured airway cells were immunostained in situ on the Trans-well membranes. Cells were fixed with 4% paraformaldehyde (PFA) for 10 min at room temperature. Non-specific antibody binding was blocked in buffer containing 3% bovine serum albumin and 0.1% TritonX100 in PBS for 1 h at room temperature. Cells were then washed with 0.1% Tween20 in phosphate buffer saline (PBS) and incubated in primary antibodies diluted in blocking buffer. Primary antibodies were anti-CCDC78 (1:100, Proteintech, 26876-1-AP), anti-CCDC33 (1:100, Santacruz, sc-390852) and acetylated alpha tubulin (mouse, Clone 6-11B- 1, 1:20.000; Sigma-Aldrich, Cat# T7451; RRID: AB_609894). After incubation at 4 °C overnight, the cells were then washed and incubated with species-specific, fluorescent-labeled secondary antibodies diluted in PBS for 45-60 min at room temperature. Membranes were mounted on glass slides in medium containing 4′, 6-diamidino-2-phenylindole (DAPI) to stain DNA (Fluoroshield, Sigma Aldrich, # F6057). Cells were imaged by wide-field fluorescent microscopy using an upright Leica 6000 microscope equipped with a cooled digital camera interfaced with imaging software (LAS X, Leica).

Mouse tissue immunostaining

The trachea and oviduct were collected from P21 mouse. Formalin-fixed and paraffin-embedded (FFPE) tissues were sectioned at 4 µm. The FFPE sections were dewaxed, rehydrated, and boiled in antigen retrieval solution Histo-VT-One (Nacarai). After blocking with Blocking-One-Histo (Nacarai), the sections were incubated with anti-CCDC78 antibody (1:100, Proteintech, 26876-1-AP) and acetylated-tubulin (1:300, Proteintech, 66200-1-Ig) overnight at 4 °C, then with Alexa Fluor-conjugated secondary antibodies (1:500, Invitrogen, A-21206, A-21203). The sections were mounted in Fluorescence-Mounting-Medium (Dako).

Immunofluorescence imaging was performed on an LSM800 confocal laser scanning microscope (Carl Zeiss).

In vitro microtubule bundling

In vitro translations of GFP, GFP-Ccdc78, and GFP-Ccdc33 proteins were performed using TnT® Coupled Wheat Germ Extract System (Promega). Briefly, 2 µg of CS10R-GFP, CS10R-GFP-Ccdc78 and CS10R-GFP-Ccdc33 plasmids were incubated with 30 µl of TnT® SP6 High-Yield Wheat Germ Master Mix in total of 50 µl reaction, 25 °C 2 h. The concentration of proteins was determined with western blot analysis by comparing translated proteins to serial dilutions of GFP peptide.

To polymerize microtubules in vitro, 2 µl of 647-labeled tubulins (2 mg/ml)(Pursolutions, 064705) were diluted in 6 µl of 1 mM GTP containing tubulin buffer (80 mM PIPES pH 6.9, 1 mM EDTA, 1 mM MgCl2, 10% glycerol). Tubulins were polymerized for 1 hour in 37 °C water bath and stabilized by adding 35 µM of Taxol solution to the polymerized microtubules. After an additional 20 minutes incubation in 37 °C water bath, microtubules were stored at room temperature, covered with foil to avoid light.

For the microtubule bundling assay, stabilized microtubules were diluted into tubulin buffer at a 1:20 dilution. 6 µl of diluted microtubules were mixed with 4 µl GFP, 4 µl GFP-Ccdc78, 4 µl GFP-Ccdc33 and 2 µl GFP-Ccdc78 + 2 µl GFP-Ccdc33. After incubation at room temperature for 20 min, 10 µl of each mixture was gently squashed

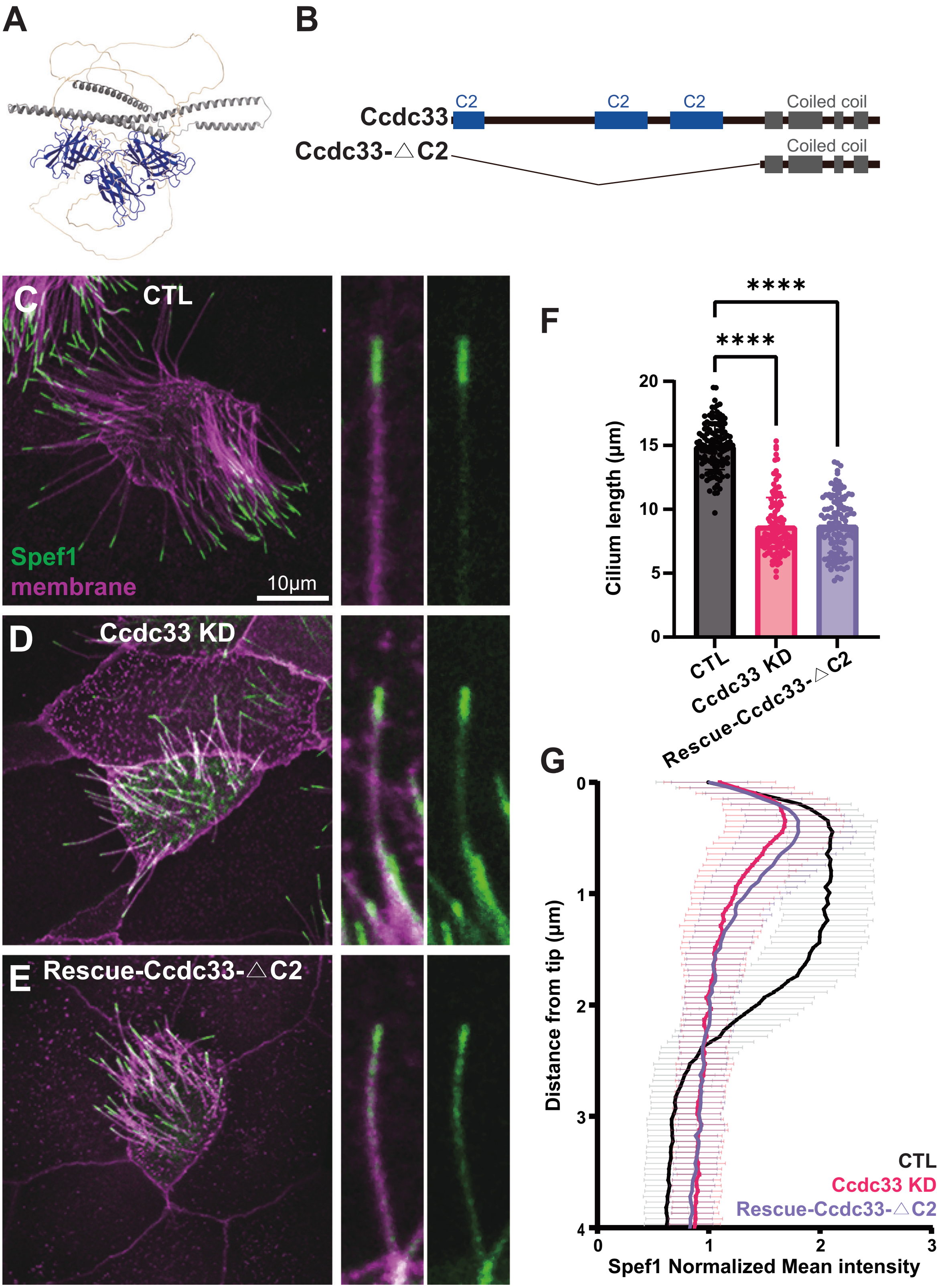

Fig. 9 | The function of C2 domain of Ccdc33 in organizing distal ciliary structure in MCC cilia. A Alphafold prediction of *Xenopus* Ccdc33 structure. C2 domain is colored in blue and coiled-coil domain in gray. **B** Secondary structure of *Xenopus* Ccdc33 and truncation of C2 domain in Ccdc33. C2 domain is colored in blue and coiled-coil domain in gray. **(C-E)** Confocal image of *Xenopus* MCC injected with GFP-Spef1 and membrane-RFP in control **C**, Ccdc33 knockdown **D** and rescue with 600 pg of *ccdc33-ΔC2* mRNA, with magnified view of cilium on the right. Scale bar represents 10 μm. **F** Quantification of the length of cilium. ****$p < 0.0001$ ($n = 120$ cilia, 40 cells, 10 embryos across 3 experiments) (Ordinary one-way ANOVA) Data are presented as mean values +/- SD. **G** Quantification of fluorescent intensity of GFP-Spef1 along the axoneme was normalized by average intensity in control, Ccdc33 MO injected and rescued with Ccdc33-△C2 embryos. ($n = 120$ cilia, 40 cells, 10 embryos, 3 experiments) Data are presented as mean values +/- SD.

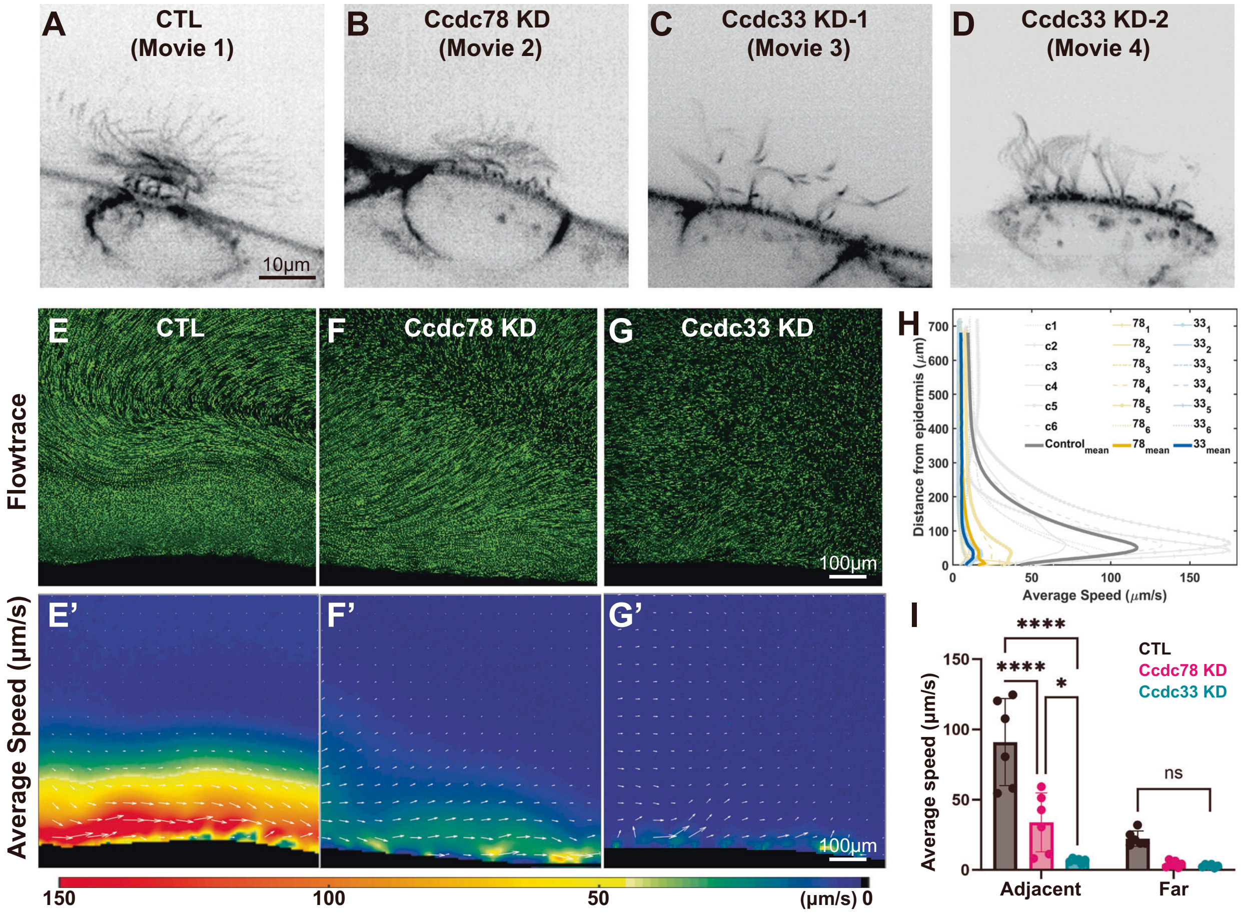

Fig. 10 | Loss of Ccdc78 and Ccdc33 elicit distinct defects in cilia beating and fluid flow. **A–D** Spinning disk microscopy image of ciliary beating in control **A**, Ccdc78 KD **B**, Ccdc33 KD-1**C** Ccdc33 KD-2**D** MCC. Scale bar represents 10 µm. **E–G** Flowtrace visualizations of one representative sample of control **E**, Ccdc78 KD **F** and Ccdc33 KD **G** with 10 seconds time averaging. Scale bar represents 100 µm. (E'-G') Speed colormap corresponding to panels 9E-G overlaid with velocity vectors (white arrows). The color scale of average speed is shown at the bottom. Scale bar represents 100 µm. **H** Speed profile graph showing average speed of fluid flow plotted as a function of distance from epidermis for all samples, with the mean values highlighted. (*n* = 6 embryos across 2 biological experiments) Data are presented as mean values +/- SD. **I** Average flow speed comparison of adjacent and far regions for all samples of control, Ccdc78 KD and Ccdc33 KD. The bar refers to the mean value, and the error bars refer to the standard errors. ****$p < 0.0001$, *$p = 0.0141$, Data are presented as mean values +/- SD. (*n* = 6 embryos across 2 biological experiments) (two-way ANOVA).

between slide glass and coverslip and sealed with VALAP (1:1:1 Vaseline: lanolin: paraffin wax).

Bead flow analysis

Xenopus embryos were grown up to stage 25–26 and mounted onto an imaging chamber in 1/3X MMR with green fluorescent beads (Fluospheres^{TM} polystyrene, 1.0 µm, yellow-green 505/515). The bead flow movies and live cilia beating videos were taken on a Nikon W1 Spinning Disc Confocal at an image rate of 40 frames per second and 80 frames per second, respectively.

Fluid flow quantification was carried out by processing a total of 18 videos, each with tracer particles live-imaged at 40 fps for a 30-second duration. The datasets included 6 videos each for control, 78KD and 33 KD. The fluid flow fields were visualized using the Flowtrace plugin in ImageJ[55] with a time window of 10 s. Further, the time-lapse image sequences were analyzed by implementing the Particle Image Velocimetry (PIV) technique using the MATLAB-based PIVlab package[56]. The velocity vectors were computed between consecutive timepoints for all the datasets using individual frames extracted from the videos (40 fps, 30 s total duration). For all the frames, the epidermis at the bottom of images was masked, and the images were pre-processed using the contrast limited adaptive histogram equalization (CLAHE) option (window size 16 pixels). The velocity vectors were computed via the FFT cross-correlation method with a first pass on 64 × 64 pixels interrogation window and the second pass on 32 × 32 pixels interrogation window with 50% overlap. Velocity vector validation was performed using appropriate velocity limits, standard deviation filters and interpolation of missing vectors.

The velocities in the directions, parallel to the epidermis and perpendicular to the epidermis, and the resultant flow speeds (velocity magnitude) were extracted at each time point. The results were calculated from the first 22.5 s of the videos (first 900 frames) for all datasets, and the remaining duration with fluctuations due to larval twitching was discarded. The fluid flow were quantified by comparison of the flow speeds averaged over time, across the area adjacent to the epidermis and far from the epidermis. The thresholds to define the adjacent region and the far region were determined to be the point of the steepest fall in flow speeds (location of minimum velocity gradient) from the epidermis. These thresholds were computed from the average speed profiles in the direction perpendicular to the epidermis, calculated by averaging flow speed over time and in the direction parallel to the epidermis. The peak and minimum flow speeds were also calculated from the average speed profile.

Alphafold3 structure prediction

The protein structure predictions were predicted by Alphafold3 using Alphafold server (https://alphafoldserver.com/).

Statistics and reproducibility

All statistical analyses and graph creation were performed in GraphPad Prism v.10.1.2. Statistical details, such as number of animals (embryos), experiments and cilia (*n*) can be found in figure legends. Each experiment was repeated at least 3 times, with the exception of the tissue immunostaining images and APMS.

Reporting summary

Further information on research design is available in the Nature Portfolio Reporting Summary linked to this article.

Data availability

The mass spectrometry data generated in this study have been deposited in the MassIVE database under accession number MSV000096822 [https://massive.ucsd.edu/ProteoSAFe/dataset.jsp?task=8be5bfd19c574151b8cc412803c166b4]. All the raw analysis data are provided in the Supplementary source data file.

References

1. Brooks, E. R. & Wallingford, J. B. Multiciliated cells. *Curr. Biol.* **24**, R973–R982 (2014).
2. Meunier, A. & Azimzadeh, J. Multiciliated cells in animals. *Cold Spring Harb. Perspect. Biol.* **8**, a028233 (2016).
3. Fliegauf, M., Benzing, T. & Omran, H. When cilia go bad: cilia defects and ciliopathies. *Nat. Rev. Mol. cell Biol.* **8**, 880–893 (2007).
4. Wallmeier, J. et al. Motile ciliopathies. *Nat. Rev. Dis. Prim.* **6**, 77 (2020).
5. Legendre, M., Zaragosi, L.-E. & Mitchison, H. M. in *Seminars in cell & developmental biol*. 19-33 (Elsevier).
6. Soares, H., Carmona, B., Nolasco, S., Viseu Melo, L. & Gonçalves, J. Cilia distal domain: diversity in evolutionarily conserved structures. *Cells* **8**, 160 (2019).
7. Dentler, W. L. & LeCluyse, E. Microtubule capping structures at the tips of tracheal cilia: evidence for their firm attachment during ciliary bend formation and the restriction of microtubule sliding. *Cell Motil.* **2**, 549–572 (1982).
8. Dentler, W. L. Attachment of the cap to the central microtubules of Tetrahymena cilia. *J. cell Sci.* **66**, 167–173 (1984).
9. Legal, T. et al. Structure of the ciliary tip central pair reveals the unique role of the microtubule-seam binding protein SPEF1. *Curr. Biol.* **35**, 3404–3417 (2025).
10. Legal, T. et al. CEP104/FAP256 and associated cap complex maintain stability of the ciliary tip. *J. Cell Biol.* **222**, e202301129 (2023).
11. Louka, P. et al. Proteins that control the geometry of microtubules at the ends of cilia. *J. Cell Biol.* **217**, 4298–4313 (2018).
12. Lechtreck, K.-F., Gould, T. J. & Witman, G. B. Flagellar central pair assembly in Chlamydomonas reinhardtii. *Cilia* **2**, 1–19 (2013).
13. Satish Tammana, T. V., Tammana, D., Diener, D. R. & Rosenbaum, J. Centrosomal protein CEP104 (Chlamydomonas FAP256) moves to the ciliary tip during ciliary assembly. *J. cell Sci.* **126**, 5018–5029 (2013).
14. Reynolds, M. J. et al. The developmental process of the growing motile ciliary tip region. *Sci. Rep.* **8**, 7977 (2018).
15. Höög, J. L. et al. Modes of flagellar assembly in Chlamydomonas reinhardtii and Trypanosoma brucei. *Elife* **3**, e01479 (2014).
16. Pratelli, A., Corbo, D., Lupetti, P. & Mencarelli, C. The distal central pair segment is structurally specialised and contributes to IFT turnaround and assembly of the tip capping structures in Chlamydomonas flagella. *Biol. cell* **114**, 349–364 (2022).
17. Dentler, W. L. Structures linking the tips of ciliary and flagellar microtubules to the membrane. *J. cell Sci.* **42**, 207–220 (1980).
18. LeCluyse, E. L. & Dentler, W. L. Asymmetrical microtubule capping structures in frog palate cilia. *J. Ultrastruct. Res.* **86**, 75–85 (1984).
19. Dirksen, E. R. & Satir, P. Ciliary activity in the mouse oviduct as studied by transmission and scanning electron microscopy. *Tissue Cell* **4**, 389–403 (1972).
20. Jeffery, P. & Reid, L. New observations of rat airway epithelium: a quantitative and electron microscopic study. *J. Anat.* **120**, 295 (1975).
21. Pedersen, L. B., Geimer, S., Sloboda, R. D. & Rosenbaum, J. L. The Microtubule plus end-tracking protein EB1 is localized to the flagellar tip and basal bodies in Chlamydomonas reinhardtii. *Curr. Biol.* **13**, 1969–1974 (2003).
22. Schrøder, J. M. et al. EB1 and EB3 promote cilia biogenesis by several centrosome-related mechanisms. *J. cell Sci.* **124**, 2539–2551 (2011).
23. Brooks, E. R. & Wallingford, J. B. Control of vertebrate intraflagellar transport by the planar cell polarity effector Fuz. *J. Cell Biol.* **198**, 37–45 (2012).
24. Konjikusic, M. J. et al. Kif9 is an active kinesin motor required for ciliary beating and proximodistal patterning of motile axonemes. *J. cell Sci.* **136**, jcs259535 (2023).
25. Zheng, J. et al. Microtubule-bundling protein Spef1 enables mammalian ciliary central apparatus formation. *J. Mol. cell Biol.* **11**, 67–77 (2019).
26. Gray, R. S. et al. The planar cell polarity effector Fuz is essential for targeted membrane trafficking, ciliogenesis and mouse embryonic development. *Nat. cell Biol.* **11**, 1225–1232 (2009).
27. Lee, C., Ma, Y., Tu, F. & Wallingford, J. B. Ordered deployment of distinct ciliary beating machines in growing axonemes of vertebrate multiciliated cells. *Differentiation* **131**, 49–58 (2023).
28. Walentek, P. & Quigley, I. K. What we can learn from a tadpole about ciliopathies and airway diseases: Using systems biology in Xenopus to study cilia and mucociliary epithelia. *genesis* **55**, e23001 (2017).
29. Tu, F., Sedzinski, J., Ma, Y., Marcotte, E. M. & Wallingford, J. B. Protein localization screening in vivo reveals novel regulators of multiciliated cell development and function. *J. Cell Sci.* **131**, jcs206565 (2018).
30. Kim, S. K. et al. A role for Cep70 in centriole amplification in multiciliated cells. *Developmental Biol.* **471**, 10–17 (2021).
31. Dehring, D. A. K. et al. Deuterosome-mediated centriole biogenesis. *Developmental Cell* **27**, 103–112 (2013).
32. Gui, M. et al. De novo identification of mammalian ciliary motility proteins using cryo-EM. *Cell* **184**, 5791–5806. e5719 (2021).
33. Kubo, S. et al. Native doublet microtubules from Tetrahymena thermophila reveal the importance of outer junction proteins. *Nat. Commun.* **14**, 2168 (2023).
34. Frikstad, K.-A. M. et al. A CEP104-CSPP1 complex is required for formation of primary cilia competent in hedgehog signaling. *Cell Rep.* **28**, 1907–1922. e1906 (2019).
35. Deblandre, A., Wettstein, G., Koyano-Nakagawa, D. A. & Kintner, N. C. A two-step mechanism generates the spacing pattern of the ciliated cells in the skin of Xenopus embryos. *Development* **126**, 4715–4728 (1999).
36. Angerilli, A., Smialowski, P. & Rupp, R. A. The Xenopus animal cap transcriptome: building a mucociliary epithelium. *Nucleic acids Res.* **46**, 8772–8787 (2018).
37. Ariizumi, T. et al. Isolation and Differentiation of Xenopus Animal Cap Cells. *Curr. Protoc. Stem Cell Biol.* **9**, 1D.5.1–1D.5.31 (2009).
38. Marquez, J., Bhattacharya, D., Lusk, C. P. & Khokha, M. K. Nucleoporin NUP205 plays a critical role in cilia and congenital disease. *Developmental Biol.* **469**, 46–53 (2021).
39. Hayes, J. M. et al. Identification of novel ciliogenesis factors using a new in vivo model for mucociliary epithelial development. *Developmental Biol.* **312**, 115–130 (2007).

40. Behnam, B., Mobahat, M., Fazilaty, H., Wolfe, J. & Omran, H. TSGA10 is a centrosomal protein, interacts with ODF2 and localizes to basal body. *J. Cell Sci. Ther.* **6**, 1 (2015).
41. Chung, M.-I. et al. Coordinated genomic control of ciliogenesis and cell movement by RFX2. *Elife* **3**, e01439 (2014).
42. Kaczmarek, K., Niedzialkowska, E., Studencka, M., Schulz, Y. & Grzmil, P. Ccdc33, a predominantly testis-expressed gene, encodes a putative peroxisomal protein. *Cytogenetic Genome Res.* **126**, 243–252 (2009).
43. Dougherty, G. W. et al. CLAMP, a novel microtubule-associated protein with EB-type calponin homology. *Cell Motil. cytoskeleton* **62**, 141–156 (2005).
44. Chateau, S., d'Ortona, U., Poncet, S. & Favier, J. Transport and mixing induced by beating cilia in human airways. *Front. Physiol.* **9**, 161 (2018).
45. Milana, E. et al. Metachronal patterns in artificial cilia for low Reynolds number fluid propulsion. *Sci. Adv.* **6**, eabd2508 (2020).
46. Bulinski, J. C., Odde, D. J., Howell, B. J., Salmon, T. D. & Waterman-Storer, C. M. Rapid dynamics of the microtubule binding of ensconsin in vivo. *J. cell Sci.* **114**, 3885–3897 (2001).
47. Woolner, S., Miller, A. L. & Bement, W. M. in *Cytoskeleton Methods and Protocols* 23-39 (Springer, 2009).
48. Kieserman, E. K., Lee, C., Gray, R. S., Park, T. J., & Wallingford, J. B. High-magnification in vivo imaging of Xenopus embryos for cell and developmental biology. *Cold Spring Harbor Protocols* **2010**, pdb. prot5427 (2010).
49. Keeling, J., Tsiokas, L. & Maskey, D. Cellular mechanisms of ciliary length control. *Cells* **5**, 6 (2016).
50. Avasthi, P. & Marshall, W. F. Stages of ciliogenesis and regulation of ciliary length. *Differentiation* **83**, S30–S42 (2012).
51. Schweickert, A. et al. Cilia-driven leftward flow determines laterality in Xenopus. *Curr. Biol.* **17**, 60–66 (2007).
52. Little, R. B. & Norris, D. P. in *Seminars in Cell & Developmental Biology*. 11–18 (Elsevier).
53. Park, T. J., Mitchell, B. J., Abitua, P. B., Kintner, C. & Wallingford, J. B. Dishevelled controls apical docking and planar polarization of basal bodies in ciliated epithelial cells. *Nat. Genet* **40**, 871–879 (2008).
54. Mitchell, B., Jacobs, R., Li, J., Chien, S. & Kintner, C. A positive feedback mechanism governs the polarity and motion of motile cilia. *Nature* **447**, 97 (2007).
55. Gilpin, W., Prakash, V. N. & Prakash, M. Flowtrace: simple visualization of coherent structures in biological fluid flows. *J. Exp. Biol.* **220**, 3411–3418 (2017).
56. Stamhuis, E. & Thielicke, W. PIVlab–towards user-friendly, affordable and accurate digital particle image velocimetry in MATLAB. *J. open Res. Softw.* **2**, 30 (2014).
57. Werner, M. E. et al. Radial intercalation is regulated by the Par complex and the microtubule-stabilizing protein CLAMP/Spef1. *J. Cell Biol.* **206**, 367–376 (2014).
58. Lacey, S. E., Graziadei, A. & Pigino, G. Extensive structural rearrangement of intraflagellar transport trains underpins bidirectional cargo transport. *Cell* **187**, 4621–4636. e4618 (2024).
59. Chien, A. et al. Dynamics of the IFT machinery at the ciliary tip. *Elife* **6**, e28606 (2017).
60. Pedersen, L. B., Geimer, S. & Rosenbaum, J. L. Dissecting the molecular mechanisms of intraflagellar transport in Chlamydomonas. *Curr. Biol.* **16**, 450–459 (2006).
61. Cho, W. Membrane targeting by C1 and C2 domains. *J. Biol. Chem.* **276**, 32407–32410 (2001).
62. Smith, D. J., Blake, J. R. & Gaffney, E. A. Fluid mechanics of nodal flow due to embryonic primary cilia. *J. R. Soc. Interface* **5**, 567–573 (2008).
63. Elgeti, J. & Gompper, G. Emergence of metachronal waves in cilia arrays. *Proc. Natl. Acad. Sci.* **110**, 4470–4475 (2013).
64. Gilpin, W., Bull, M. S. & Prakash, M. The multiscale physics of cilia and flagella. *Nat. Rev. Phys.* **2**, 74–88 (2020).
65. Cui, Z., Wang, Y. & den Toonder, J. M. Metachronal motion of biological and artificial cilia. *Biomimetics* **9**, 198 (2024).
66. Goldstein, R. E., Polin, M. & Tuval, I. Noise and synchronization in pairs of beating eukaryotic flagella. *Phys. Rev. Lett.* **103**, 168103 (2009).
67. Solovev, A. & Friedrich, B. M. Synchronization in cilia carpets and the Kuramoto model with local coupling: Breakup of global synchronization in the presence of noise. *Chaos: An Interdisciplinary Journal of Nonlinear Science* **32**, https://doi.org/10.1063/5.0075095 (2022).
68. Majczenko, K. et al. Dominant mutation of CCDC78 in a unique congenital myopathy with prominent internal nuclei and atypical cores. *Am. J. Hum. Genet.* **91**, 365–371 (2012).
69. Eker, D. et al. Investigating the genetic etiology of pediatric patients with peripheral hypotonia using the next-generation sequencing method. *Glob. Med. Genet.* **9**, 200–207 (2022).
70. Uhlén, M. et al. Tissue-based map of the human proteome. *Science* **347**, 1260419 (2015).
71. Karlsson, M. et al. A single–cell type transcriptomics map of human tissues. *Sci. Adv.* **7**, eabh2169 (2021).
72. Goyal, N., Waldrop, M. & Mozaffar, T. Unique myopathy presenting in adulthood with proximal muscle weakness and respiratory insufficiency. *Neuromuscul. Disord.* **25**, S282 (2015).
73. Lopergolo, D. et al. CCDC78: unveiling the function of a novel gene associated with hereditary myopathy. *Cells* **13**, 1504 (2024).
74. Horani, A. & Ferkol, T. W. Understanding primary ciliary dyskinesia and other ciliopathies. *J. Pediatr.* **230**, 15 (2020).
75. Shapiro, A. J. & Leigh, M. W. Value of transmission electron microscopy for primary ciliary dyskinesia diagnosis in the era of molecular medicine: Genetic defects with normal and non-diagnostic ciliary ultrastructure. *Ultrastructural Pathol.* **41**, 373–385 (2017).
76. Goodman, J. K., Zampronio, C. G., Jones, A. M. & Hernandez-Fernaud, J. R. Updates of the in-gel digestion method for protein analysis by mass spectrometry. *Proteomics* **18**, 1800236 (2018).
77. Huerta-Cepas, J. et al. eggNOG 4.5: a hierarchical orthology framework with improved functional annotations for eukaryotic, prokaryotic and viral sequences. *Nucleic acids Res.* **44**, D286–D293 (2016).
78. Brody, S. L. et al. Undocking of an extensive ciliary network induces proteostasis and cell fate switching resulting in severe primary ciliary dyskinesia. *Sci. Transl. Med.* **17**, eadp5173 (2025).
79. Horani, A. et al. Establishment of the early cilia preassembly protein complex during motile ciliogenesis. *Proc. Natl. Acad. Sci. USA* **115**, E1221–E1228 (2018).
80. Horani, A., Nath, A., Wasserman, M. G., Huang, T. & Brody, S. L. Rho-associated protein kinase inhibition enhances airway epithelial Basal-cell proliferation and lentivirus transduction. *Am. J. Respir. Cell Mol. Biol.***49,** 341–347 (2013).

Acknowledgements

J.B.W. is supported by the NHLBI (R01HL117164); J.H. was supported by the Korea Health Technology R&D Project through Korea. Health Industry Development Institute (KHIDI), funded by the Ministry of Health & Welfare, Republic of Korea (grant number: HI19C1095). EMM was supported by the NIGMS (R35GM122480), Army Research Office (W911NF-12-1-0390), and the Welch Foundation (F-1515). AH was supported by the (NHLBI R01HL173490). S.B. was supported by the NHLBI (HL146601, HL128370). TJP is supported by the Institute for Basic Science (IBS-R022-D1) and the Korean National Research Foundation (grant number: RS-2023-00225555, RS-2024-00335111). VNP was supported by startup funding from the University of Miami.

Author contributions

J.H. and C.L. performed the project, carried out experiments, and analysis. O.P. performed proteomic analysis. G.M. performed bead flow analysis. E.A. performed *Xenopus* bead flow movie acquisition. G.H. performed TEM image acquisition. J.P. performed human cell experiments. M.T. performed mouse tissue experiments. N.I.M. helped in vitro microtubule polymerization experiments. D.J.D., A.H., S.L.B., E.M.M., and V.N.P. supervised elements of the project and acquired funding. T.J.P. and J.B.W. directed and supervised the project and assembled the manuscript.

Competing interests

The authors declare no competing interests.

Additional information

Supplementary information The online version contains supplementary material available at https://doi.org/10.1038/s41467-025-67086-9.

Correspondence and requests for materials should be addressed to Tae Joo Park or John B. Wallingford.

Peer review information *Nature Communications* thanks the anonymous reviewers for their contribution to the peer review of this work. A peer review file is available.

Reprints and permissions information is available at http://www.nature.com/reprints

Publisher's note Springer Nature remains neutral with regard to jurisdictional claims in published maps and institutional affiliations.